

ON THE ENHANCEMENT OF BIODIESEL DROPLET VAPORISATION USING ELECTROSTATIC CHARGE

By

Tushar Ahmed

B.Sc., Chittagong University of Engineering and Technology, Bangladesh, 2011

M.Sc., University of Ulsan, South Korea, 2016

A THESIS SUBMITTED TO MACQUARIE UNIVERSITY

FOR THE DEGREE OF MASTER OF RESEARCH

SCHOOL OF ENGINEERING

19 OCTOBER 2017



MACQUARIE
University
SYDNEY • AUSTRALIA

The work presented in this thesis was carried out at the School of Engineering, Macquarie University, Sydney, Australia, between January 2017 and October 2017. Except where acknowledged in the customary manner, the material presented in this thesis is, to the best of my knowledge, original and has not been submitted in whole or part for a degree in any university.

Tushar Ahmed

Acknowledgements

After an intensive period of nine months, writing this note of thanks is the finishing touch to my Master of Research Degree at Macquarie University. It has been a period of profound learning for me, not only in the scientific arena but also on a personal level. I would like to reflect on the people who have supported and helped me so much throughout this period.

First and foremost, my deepest gratitude goes to my adjunct supervisor Dr Agissilaos Kourmatzis, for his unwavering support, encouragement, and mentorship throughout this project. Without his guidance, this work would not have been possible. I would like to extend my gratitude to my principal supervisor Dr Sammy Diasinos for his cooperation. I am also incredibly thankful to Dr Keith Imrie, for helping me in eradicating grammatical mistakes.

Personally, I am thankful to my elder brother Mohammad Masum, for his wise counsel and a sympathetic ear. More personal thanks are due to my friends, for helping me to maintain a balance between academic and social life. Finally, special thanks and cordial love to Rokeya Nasrin, for her constant support, prayers, and encouragement, which allowed me to start and complete this academic task.

Nomenclature

General

B	Magnetic Field	Vs/m^2
D	Diameter	m
E	Electric Field	V/m
f	Force	N
g	Gravitational acceleration	m/s^2
P	Pressure	Pa
t	Time	s
T	Temperature (scalar)	K

Acronyms

DI	Direct Injection
DNS	Direct Numerical Simulation
EHD	Electrohydrodynamics
FAME	Fatty Acid Methyl Ester
IC	Internal-combustion
PM	Particulate Matter
SOF	Soluble Organic Fraction

Non-dimensional numbers

C	Injection Strength
M	EHD ‘M’ Number
Nu	Nusselt Number

Pr	Prandtl Number
Re	Reynolds Number
Re_E	Electric Reynolds Number
Sc	Schmidt Number
T	Electrical Rayleigh Number

Greek

ρ	Density	Kg/m^3
μ	Dynamic Viscosity	Pa.s
Δ	Difference	
β	Evaporation Parameter	
k	Ionic Mobility	m^2/Vs
ν	Kinematic Viscosity	m^2/s
ε	Permittivity of Vacuum	F/m
η	Rayleigh Limit Coefficient	
σ	Surface Tension	N/m
τ	Time Scale	s

Abstract

An electrostatic atomiser is an energy-efficient device that can be used to promote the atomisation of highly viscous fluids, for example biodiesel. It imposes an electrical charge onto the liquid that creates enough Coulombic repulsive force to lower the surface-tension force of the liquid and result in atomisation.

In this study, the vaporisation of electrically charged fatty-acid methyl-ester (FAME) droplets are reported as a function of the initial charge density, ambient temperature, and droplet Reynolds number. Existing data from a direct numerical simulation (DNS) of charge injection are also post-processed to better understand the physics of electro-convection as a function of the average bulk-flow velocity and the electrical Rayleigh number.

The model predictions are assessed by comparing with experimental results, and the maximum deviation in evaporation time is reported to be 13.6% for C12:0. The effect of charge increases with increasing initial charge density and decreases at high ambient temperatures, while the droplets Reynolds number shows a mixed effect. The DNS data processing reveals that the developed electro-convective instabilities force the liquid into a roll-like structured motion and in a high-flow-rate atomiser, higher instability could maximise the amount of charge in the middle of the domain.

List of Publications

- Tushar Ahmed and Agisilaos Kourmatzis, *On the enhancement of biodiesel droplet vaporization using electrostatic charge*, 11th Asia-Pacific Conference on Combustion, The University of Sydney, NSW 2006, Australia, 10th -14th December 2017(Accepted).

Contents

Acknowledgements	v
Nomenclature	vii
Abstract	ix
List of Publications	xi
List of Figures	xvii
List of Tables	xix
1 Introduction	1
1.1 Motivation and Objectives	1
1.2 Organisation of the thesis	4
2 Literature Review	5
2.1 Introduction	5
2.2 Evaporation models for a single biodiesel droplet	6
2.2.1 Biodiesel as a single-component fuel	6
2.2.2 Biodiesel and its constituent components	9
2.3 Electrostatic atomiser	10
2.4 Chapter summary	13

3	Methodology	15
3.1	Introduction	15
3.2	Model formation	15
3.2.1	Assumptions	16
3.2.2	The governing equations	16
3.2.3	Fuel Properties	18
3.3	Solution approach	19
3.4	Evaporation of charged droplet	22
3.4.1	Charge-only case	22
3.4.2	Charge and combustion case	23
3.5	Chapter summary	24
4	Results and Discussion	27
4.1	Introduction	27
4.2	Model validation	27
4.3	Model predictions	28
4.3.1	Effect of initial charge density	29
4.3.2	Effect of ambient temperature	30
4.3.3	Effect of Reynolds number	33
4.4	Chapter summary	34
5	EHD flow inside the atomiser	37
5.1	Introduction	37
5.2	Theoretical study	38
5.3	Governing equations	39
5.4	Charge distribution analysis	42
5.4.1	Effect of electrical Rayleigh number (T)	43
5.4.2	Effect of average bulk-flow velocity (U_{av})	43
5.5	Chapter summary	44

6	Conclusions and future work	49
6.1	Introduction	49
6.2	Main Findings	50
6.2.1	The effect of charge on FAMEs' droplet vaporisation	50
6.2.2	The charge distribution between the electrodes	50
6.3	Future work	51
A	Appendix	53
	References	65

List of Figures

2.1	D^2 versus time curve for two different fuels. Initial conditions are: $T_g = 420^\circ$ C, $D = 1.62$ mm, $T_d = 25$ K, $R_e = 0$, and $P_\infty = 1$ atm. Reprinted from Fuel, Volume 90, W.L.H. Hallett, N.V. Legault, Modelling biodiesel droplet evaporation using continuous thermodynamics, pages 1221-1228, Copyright (2017), with permission from Elsevier.	7
2.2	(a) Version one, (b) Version two, and (c) Version three of electrostatic atomiser.	12
3.1	Schematic of a charged droplet fragmentation, evaporation, and combustion process.	22
3.2	Flowchart showing the steps of fragmentation of a core droplet into a residual and n siblings and their contribution towards the droplet vaporisation. . . .	25
4.1	Comparison between the predictions of the present model and experimental findings for the D^2 versus time history of FAMEs. Initial conditions are: $T_g = 420^\circ$ C, $D = 1.62$ mm, $T_d = 25$ K, $R_e = 0$, and $P_\infty = 1$ atm.	28
4.2	D^2 history for a Stearate (C18:0) droplet with no charge, with charge and no reaction, and with charge and reaction for $n = 5$; Initial conditions are: $D = 0.001$ m, $T_g = 600$ K, $T_d = 298$ K, $R_e = 0$, and $Q_i/Q_{ray} = 0.7$	29
4.3	Vaporisation time difference versus initial charge density factor (Q_i/Q_{ray}) for charge and reaction cases with $n = 5$. Initial conditions are: $D = 0.001$ m, $T_g = 700$ K, $T_d = 298$ K, and $R_e = 0$	30

4.4	Vaporisation time difference versus ambient temperature for various FAMEs with no-charge and charge cases. Initial conditions are: $D = 0.001$ m, $T_d = 298$ K, $R_e = 0$, and $Q_i/Q_{ray} = 0.7$	31
4.5	Mass fraction of the vapour at droplet surface versus ambient temperature for all the FAMEs. Initial conditions are: $D = 0.001$ m, $T_d = 298$ K, $R_e = 0$, and $Q_i/Q_{ray} = 0.7$	32
4.6	Vaporisation time difference versus ambient temperature with charge and re-action cases for $n = 5$. Initial conditions are: $D = 0.001$ m, $T_d = 298$ K, $R_e = 0$, and $Q_i/Q_{ray} = 0.7$	33
4.7	Evaporation constant versus ambient temperature for various FAMEs with no charge. Initial conditions are: $D = 0.001$ m, $T_d = 298$ K, $R_e = 0$, and $Q_i/Q_{ray} = 0.7$	34
4.8	Vaporisation time difference versus Reynolds number with charge and reaction cases for $n = 5$. Initial conditions are: $D = 0.001$ m, $T_d = 298$ K and $Q_i/Q_{ray} = 0.7$	35
5.1	Schematic of a typical electrostatic atomiser.	38
5.2	Typical flow pattern of insulating liquid through two parallel plates.	39
5.3	Boundary conditions and solution domain.	42
5.4	Normalised space-charge distribution as a function of T and U_{av}/kE	45
5.5	Distribution of normalised space charge in vertical locations as a function of T and U_{av}/kE	46
5.6	Spatially averaged normalised space charge versus normalised time as a function of T and U_{av}/kE	47

List of Tables

2.1	Various convection correlations	8
3.1	Coefficient values for (3.11-3.17)	20
3.2	Properties of FAMEs	21

1

Introduction

1.1 Motivation and Objectives

The dependence on fossil fuels with their contributions to ambient air pollution, especially the soluble organic fraction (SOF) and the particulate matter (PM), has already become a major problem worldwide. Some ingredients of SOF cause mutagenic and /or carcinogenic outcomes [1], whereas PM creates acute and chronic problems for the human body's respiratory tract and the cardiovascular system [2]. Moreover, burning of fossil fuels multiplies greenhouse-gas emissions, and the ever-increasing usage of internal-combustion (IC) engines dramatically enhances this greenhouse impact. To mitigate this situation an alternative to diesel fuel, such as the development of biodiesel fuels is envisaged [3–5].

Triglycerides, which are the major components of vegetable oils or animal fats, are subjected to a chemical reaction in the presence of alcohol and this process leads to the creation

of biodiesel fuels [5]. It has a higher cetane number and similar or greater energy density than diesel fuel. Also, biodiesel possesses two oxygen atoms per molecule and often one or more double bonds, which makes it more beneficial. The presence of excess oxygen in the molecule reduces both carbon-monoxide formation and particulate-matter discharge [6]. Apart from these, the biggest advantage that biodiesel offers is the reduction in carbon-dioxide emissions. According to Hill et al. [7], the same engine running on biodiesel can decrease its greenhouse-gas emissions by 40% compared with diesel fuel. However, as with all other plant oils, it also has a much higher viscosity than diesel fuel, which creates challenges for direct injection (DI) engines to obtain efficient atomisation.

In general, a conventional fuel-injection system requires a range of 1500 to 7000 psi pressure to generate 10 to 100 μm droplets [8]. However, those droplets are not uniform in size, and the formation of small droplets in the tail section increases the likelihood of droplet coalescence. Subsequently, the demand for a fine spray with precise droplet distribution creates an opportunity to find a possible replacement for these high-pressure fuel injectors. A possible list of injectors capable of replacing the conventional technology comprises air blast, effervescent, ultrasound, and electrostatic atomisers. Of these, due to its wider operating range (≥ 0.5 bar) and lower power consumption (2 – 250 mW), the electrostatic atomiser is attracting much interest. It operates by introducing an electrical charge into a bulk liquid jet such that Coulombic repulsion can assist in the liquid-fragmentation process. These devices can not only help to atomise highly viscous liquids but can also reduce the total vaporisation time of a fuel droplet [9, 10]. In addition, for small engines (20 – 250 cc), where the required pressure for generating an efficient atomisation is not available, the electrostatic atomiser is a preferable option [11]. Additionally, it encourages control over the droplet size, their motions and trajectories, by adjusting the applied electrical voltage. The generated Coulombic repulsion also prevents agglomeration among droplets and produces a uniform space distribution.

In the last three decades, considerable research has been carried out to develop charge-injection atomisers working with insulating liquids such as diesel and kerosene. With the aim of increasing the spray's specific charge, several modifications to nozzle design have been made [12–14]. The type of electrodes, the distance between the electrode and the ground

plate, and the orifice diameter have undergone optimisation to: firstly, maximise the spray's specific charge; and secondly, minimise the amount of current lost or leaked to the atomiser housing [15–17]. However, the use of bio-oils as a working liquid in a charge-injection atomiser has rarely been reported in the literature [10, 18]. In the case of biodiesels, which are largely electrically insulating dielectrics, and considering all of their constituent components, there has been no detailed documentation in the literature to date focusing on the influence of electrostatic charge in a charge-injection atomiser. For this reason the overarching objective of this project is to check the viability of using charge-injection atomisers for biodiesel fuel.

To do that, three main goals established for this study are to: (1) investigate the effects of electrical charge on droplet vaporisation for various fatty acid methyl esters (FAMES); (2) optimise effective key parameters such as initial charge density, ambient temperature and droplet Reynolds number to achieve efficient atomisation; and (3) increase the fundamental understanding of electrohydrodynamic (EHD) flow inside the atomiser.

(1) To accomplish the first goal, a previously developed and validated evaporation model (for both the conditions, i.e. without and with charge on the droplet surface) for simpler fuels is extended to calculate the total vaporisation time for a single droplet of an individual FAME. The outcomes of the extended model are then validated against experimental findings. Thereafter, the response in droplet vaporisation with respect to surface charge for an individual FAME is analysed.

(2) To accomplish the second goal, key parameters were numerically investigated for various ranges to quantify their effects on the enhancement of vaporisation. Three questions are addressed: firstly, what initial charge density gives a shorter evaporation timescale; secondly, what is the relationship between ambient temperature and the effect of charge with an increasing number of carbon and double bonds; and thirdly, how does the droplet Reynolds number influence the vaporisation time?

(3) For the third goal, existing data from a 2D direct numerical simulation for a dielectric fluid flowing through two parallel plates is post-processed. The aim here is to express the charge distribution as a function of the average bulk-flow velocity and the stability parameter.

1.2 Organisation of the thesis

This thesis is structured into six chapters. Chapter 2 reviews the recent work that has been done on droplet vaporisation modelling of biodiesel fuels. This chapter also covers contributions to electrostatic atomiser development to date. Chapter 3 provides the related assumptions, governing equations, and solution approach to the droplet vaporisation model implemented in this thesis. Details of fuel properties needed to be calculated for biodiesel fuel, and an explanation of the charged droplet breakup mechanism is also highlighted in this chapter. Chapter 4 reports the outcomes of the model based on chosen variables. In Chapter 5, the basics of the charge transportation and their distribution using various non-dimensional numbers are explained. Finally, Chapter 6 concludes the main findings and suggests avenues for future research to pursue on this topic.

2

Literature Review

2.1 Introduction

This chapter is divided into two main sections, of which the first part summarises the research carried out over the last decade on biodiesel droplet vaporisation modelling approaches. This investigation is also split into two further subsections, one based on the consideration of biodiesel as a single-component fuel, and the other taking into account its constituent components. The latter section provides a review of the gradual development of the electrostatic atomisation technique thus far.

2.2 Evaporation models for a single biodiesel droplet

Droplet vaporisation is always important for combustion processes. In practice, the liquid jets first break into droplets of varying dimensions and form a spray region; the fuel drops absorb heat from the surrounding hot gases and vaporise, then mix with the air, and combustion occurs. The whole process largely depends on the mole fraction in the vapour phase to determine the position of the flame and the amount of heat release. This complicated process for a single biodiesel droplet has been numerically studied by several authors in the last decade [19–25]. Most of the models consider the biodiesel as a single-component fuel while others observe the vaporisation process that take into account the elements of the fuel.

2.2.1 Biodiesel as a single-component fuel

Barata et al. [19] presented a mathematical model where an unstable cross-stream was employed to inject biofuel droplets. The authors showed that the mass at the droplet surface was strongly related to the type of fuel used. They argued that preheating is necessary to obtain a completely homogeneous mixture, and ethanol is more suitable for spark ignition units, whereas the use of rapeseed methyl esters can be beneficial in diffusion flame-utilisation systems. The authors found that, for both diesel and rapeseed methyl-ester fuels, the fuels did not reach an equilibrium condition in the first 50 ms. Both the fuels take time for pre-heating and this is called the evaporation starting time. The authors also observed two different mass-fraction criteria for the same fuel with and without preheating.

Hallett et al. [20] developed a numerical model to predict droplet evaporation time based on continuous mixing theory. The main advantage of their modelling approach was the elimination of the details of chemical composition. They divided biodiesel fuel into three different groups: (1) saturated, (2) one degree of unsaturation, and (3) two degrees of unsaturation. Their findings illustrate that, for a long chain, the degree of unsaturation influences the droplet evaporation timing slightly. They used two different types of fuel in their modelling and named them sample 1 and sample 2. The authors conducted their experiment three to six times and plotted the average values. In the property calculation, they used the 1/3rd rule. In the experiment, droplets for all the fuels initially increase in

size over time; this is a result of thermal expansion. Their findings on droplet evaporation history for an ambient temperature of 420 degrees Celsius are illustrated in Fig. 2.1 [20], from which it is evident that the model predicts sample 2 results more accurately than for

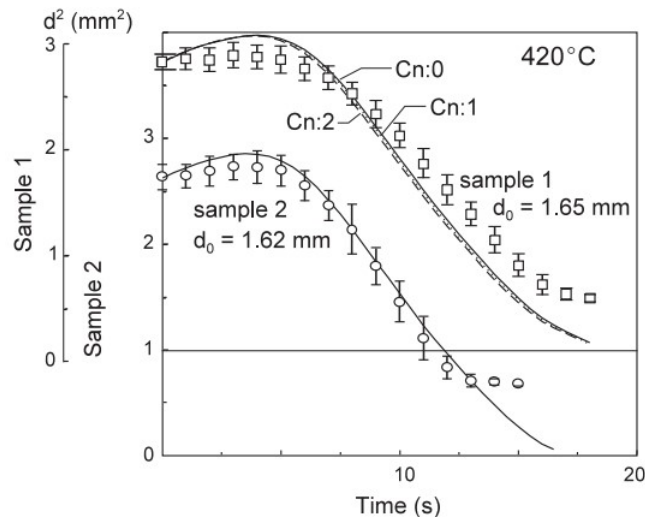


FIGURE 2.1: D^2 versus time curve for two different fuels. Initial conditions are: $T_g = 420^\circ \text{C}$, $D = 1.62 \text{ mm}$, $T_d = 25 \text{ K}$, $R_e = 0$, and $P_\infty = 1 \text{ atm}$. Reprinted from Fuel, Volume 90, W.L.H. Hallett, N.V. Legault, Modelling biodiesel droplet evaporation using continuous thermodynamics, pages 1221-1228, Copyright (2017), with permission from Elsevier.

sample 1. Here, Cn:0, Cn:1, and Cn:2 represent groups of fatty acids with no double bonds, a single double bond and two double bonds respectively. From Fig. 2.1, furthermore, it seems that all three groups follow the same path both in practice and in modelling.

Saha et al. [21] proposed a multicomponent evaporation model for high-temperature environments. They used both pure and mixed forms of biodiesel to analyse the evaporation behaviour in a real combustion system. They calculated the physical properties the same way as Hallet et al. [20] and claimed that the evaporation rate is quite slow for pure biodiesel compared with pure diesel fuel. In blending, the droplet surface temperature increased proportionally with the amount of biodiesel. At environmental pressure and 800 K temperature, internal boiling inside the mixing biodiesel droplets was observed. The authors made five assumptions for simplifying the modelling procedure. The gas flow is assumed to be one-dimensional, and initially droplets travel on the same path. The thermal diffusivity in the vapour was assumed to be higher than that of the liquid. Both the phases (liquid

and gas) maintained an equilibrium situation. The authors neglected the effect of pressure dispersal and the flow was assumed to be Stefan flow.

Dirude et al. [22] suggested a single-droplet evaporation model based on infinite-thermal-conductivity theory. The authors executed their simulation for a chosen range of ambient temperatures (550-1050 K) at a constant pressure of 0.1 MPa. They used the five different convection correlations listed in Table 2.1 [22] and made a comparison of them.

Abbreviations	TABLE 2.1: Various convection correlations Correlations
C1	$Nu = 2 + 0.552(Re_d)^{1/2}(Pr_g)^{1/3}$
C2	$Nu = 1 + (1 + Re_d Pr_g)^{1/3} f(Re_d)$
C3	$Nu = 2 + 0.552(Re_d)^{1/2}(Pr_g)^{1/3} (1 + \frac{1.232}{Re_D(Pr_g)^{4/3}})^{-1/2}$
C4	$Nu = \frac{2+0.87(Re_d)^{1/2}(Pr_g)^{1/3}}{(1+B_M)^{0.7}}$
C5	$Nu = \frac{2+0.39(Re_r)^{0.54}(Pr_g)^{0.76}}{(1+B_M)^{0.557}}$

The authors adopted the following equation [22] to calculate the fuel properties:

$$\phi_{g/m} = Y_{A,ref}(\phi_a | at, T_{ref}) + Y_{F,ref}(\phi_{v|at, T_{ref}}) \quad (2.1)$$

where ϕ can be C_p , k , or μ . The authors stated that for rapeseed methyl ester the correlation C_1 was best suited to the experimental values. For sunflower methyl ester, at an ambient temperature $T_{amb} \geq 590$ K, both the correlations C_1 and C_2 predict almost the same values as the experimental ones. The authors used the boiling-point temperature in order to calculate critical properties of their testing fuels, and the infinite-conductivity model in their mathematical modelling. For the droplet shape, phase equilibrium, and surrounding fluid, the authors assumed the same as Saha et al.[21].

Azami et al. [23] studied droplet evaporation modelling for six different fuels, kerosene, ethanol, methanol, microalgae biofuel, jatropha biofuel, and camelia biofuel to investigate their transient behaviour. The authors identified that vapour pressure is an important key parameter for defining the transient shape of vaporisation. They retained the initial conditions and did not change them for all the chosen fuels. All the fuel droplets were found to

have experienced thermal diffusion. The authors also found that at a higher initial temperature the droplet diameter becomes very small and the particle velocity is also reduced. The authors pointed out that, at a very high velocity of particles, the time taken for evaporation remains constant and the drag was also higher. Conversely, at a very low velocity, the length of penetration increased.

2.2.2 Biodiesel and its constituent components

Sazhin et al. [24] determined the droplet heating and evaporation behaviour of biodiesel fuel in a similar environment as that for a diesel engine. The authors took into account the temperature gradient and re-circulation within the droplet in their modelling approach. They used four different types of biodiesel fuels and calculated the evaporation time in two different ways: firstly, considering elements up to C16, and assuming a single-component fuel by averaging transport; and secondly, the thermodynamic properties. The authors showed that both approaches predict almost the same evaporation time with a difference of about 5.5%. For diesel and gasoline fuels, the difference in predictions when utilising both approaches was much smaller.

Qubeissi et al. [25] made a comparison of four different models using nineteen different types of biodiesel fuels. Initially, they took into account all the components of biodiesel fuels and also assumed realistic diffusion. In their second approach they again considered all the components but the diffusion was set to be infinitely fast. The authors neglected the transient diffusion in their third approach. Lastly, they extended their third model considering the fuel as a single component like Sazhin et al. [24]. They found that the model, when taking account the effects of finite diffusivity and conductivity, calculated the evaporation rate 15% more accurately than the others. For rapeseed methyl-ester, the second model under-predicts the evaporation rate with values of 15.1% compared to the first model. The single-component model calculated the evaporation rate much accurately than the third model. Besides, multicomponent models computed a higher surface temperature than with single-component models.

2.3 Electrostatic atomiser

The working principle of a pressure-driven fuel injector is to make the shear layer unstable, which forces the liquid jet to break up into droplets. However, fuels having a higher kinematic viscosity, like biodiesel, suppress this shear-layer instability. The traditional fuel injector as mentioned in the motivation section, also has less control over droplet size and droplet agglomeration, and therefore the demand for an appropriate replacement is acknowledged. The electrostatic atomiser is a device which can overcome the difficulties as mentioned above. The main advantages that it offers are controllability of droplet size, wider operating pressure range, and economy in power consumption.

In the electrostatic atomisation process an electrostatic force is applied to break up the liquid jet, rather than hydrodynamic pressure as used in conventional pressure-driven injectors. The process starts with the working fluid passing through the inter-electrode gap. A high negative voltage is added to the emitter electrode while the collector electrode remains grounded. The liquid starts getting charged and, at a value higher than the threshold level, the presence of like charges creates enough electrical force to exceed the surface-tension force, resulting in atomisation. The charge-transfer mechanism for insulating liquids is still an ongoing discussion. There are two available explanations. A field-emission mechanism is one of them which suggests [26] that, depending on the working fluid's resistivity, electrons from the applied voltage are transmitted into the fluid surface at high intensities ($\sim 10^8$ V/m). The second theory [26], which is more acceptable, suggests that a series of electro-chemical reactions allow charges to get into the fluid surface. This implies that charge transportation occurs due to dissolved ions rather than to carriers present in the liquid-metal interface.

In the context of developing an energy-efficient atomising device, in 1975 the first experimental work for generating small droplets of insulating liquid (Freon 113) was conducted by Kim and Turnbull [27]. The authors used a sharp tungsten needle as a high positive-voltage source and noted that increases in both the fluid flow rate and applied voltage resulted in reducing the droplet diameter. However, the presence of insufficient current ($\sim 10^{-9}$ A) in the liquid and a low flow rate ($\sim 10^{-3}$ mL/s) were the main drawbacks of that method. Later on, Robinson et al. [13] used both positively and negatively charged needles to inject

ions into silicone oil with a conductivity of 10^{-12} S/m. The authors claimed that a needle tip with a radius of less than 10^{-6} m was able to produce a fine spray for applied electrical intensities of 5×10^9 V/m or ionisation field intensities of 5×10^{10} V/m.

In 1984, Kelly [28] introduced his spray-triode concept. He brought the ground plate near the needle tip and discovered that an emitter with a radius less than 1μ m and made from UO_2 could operate with a flow rate of 1 mL/s. The amount of charge emitted per injection can be denoted as the total current, which is the summation of the current carried by the droplet and the current going to the ground plate.

Research on an electrostatic atomiser with a point-plane structure was then continued by Shrimpton and Yule [29]. The authors demonstrated that a special material for the needle tip is not necessary. They were also able to produce a maximum spray specific charge of 3 C/m^3 using a stainless-steel needle tip of 150μ m diameter for a fluid velocity of 26 m/s. Shrimpton and Yule used two different versions of charge injectors, namely version one and version two. The authors ran their experiment with three different types of working fluids (white spirit, kerosene, diesel oil) and a negative voltage up to 30 kV [29]. The inner structure of the version-one nozzle designed by Jido can be found in [30]. In version one, the atomisation performance was poor. Shrimpton and Yule pointed out that the poor atomisation occurred due to the large distance between the charge emitter and the ground plate. To address this issue, in version two a structural modification was made. They brought the ground plate much closer to the charge emitter and reduced the orifice diameter. Consequently, they were successful in generating a higher specific charge with values of 2 C/m^3 against 0.5 C/m^3 in version one [29]. However, two possible electrical-breakdown flow regimes were marked out by the authors, termed ‘subcritical’ and ‘supercritical’. In the subcritical flow, the bulk flow rate decreases and the injected current recirculates inside the atomiser causing the fuel to lose its insulating property. On the other hand, in the supercritical flow, the bulk flow rate is high enough to create a corona discharge outside of the atomiser.

A further structural development carried out by Rigit and Shrimpton [14] is formally known as the third version. They implemented a design to control the position of the needle tip. The authors did their experiments for a variety of orifice diameters and viscosities of the fluids. The flexibility in positioning of the needle tip and the smaller orifice diameter

allowed them to obtain a higher specific charge, in fact 26% more than that of version two. The authors also noted the involvement of the operating liquid's physical properties for influencing the injection process, and confirmed the existence of possible breakdown regimes as mentioned by Shrimpton and Yule. Fig.2.2 illustrates a comparative view of all three versions of the point-plane electrostatic atomiser.

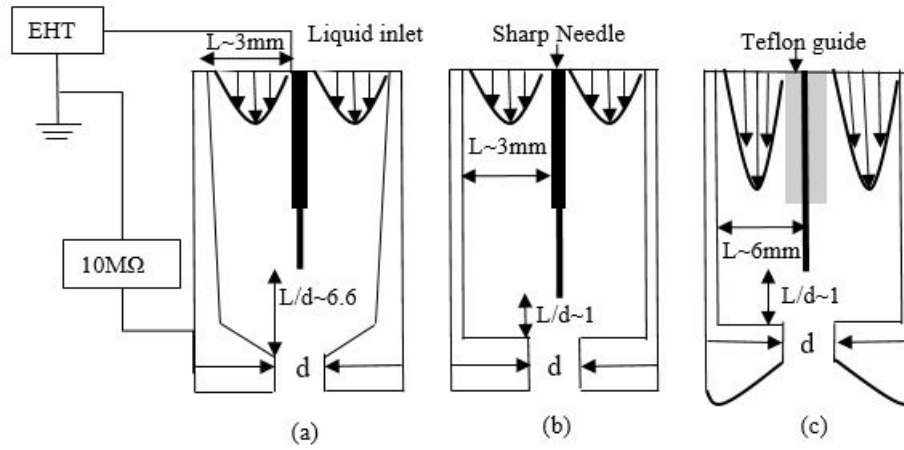


FIGURE 2.2: (a) Version one, (b) Version two, and (c) Version three of electrostatic atomiser.

Al Ahmad et al. [10] conducted an experimental study on highly viscous biofuels using virtually the same injector as employed by Rigit et al. [14]. The only difference in their experimental setup was the tip radius. They examined the amount of current received by the ground plate, the spray breakup mechanism, and spray penetration for the chosen fuels, and compared it to the conventional diesel fuel. The authors confirmed electrostatic atomisation as a valid method for producing sprays of biofuels. The authors also found biofuels capable of producing the same specific charge as with diesel fuel for all the varying key parameters. However, an atomiser working with biofuel required a higher voltage. Variations were also found in the jet breakup and atomisation processes.

Apart from the point-plane structure, Allen et al. [31] proposed a multiple-orifice geometry in 2005. The main idea was to increase the flow rate with a constant pressure by increasing the number of orifices. The authors introduced a high-voltage emitter electrode surface instead of a needle tip as an electrode. This structure not only allows a reduced orifice diameter but also helps to overcome the needle-tip alignment issue. The main advantage

of using a multiple-orifice electrode surface is the high internal bulk flow velocity around the electrode tip. It helps the spray to carry a charge when leaving the injector.

Malkawi [32] studied experimentally this multiple-orifice structured injector. The author investigated the performance based on key parameters such as orifice size and pattern, and the gap between the electrode and nozzle surface. The author's findings can be summarised as follows: the spray's specific charge increases with an increasing fluid flow rate and reducing orifice size [32] such that the efficiency of spray charges declines in multiple-orifice atomisers.

In other research the multiple-orifice high-voltage electrode was also examined by Kourmatzis et al. [33]. The authors conducted an experimental study using this multi-orifice injector with a diamond-faced electrode and compared their results with a conventional point-plane injector. They concluded that this injector is able to produce a higher electrical efficiency for a lower operating voltage. In addition, the specific charge also increases with the flow rate. However, as a result of using a higher number of holes, a loss in specific charge was observed by the authors and this was consistent with the finding by Malkawi [32].

Kourmatzis [11] continued his research on the multi-orifice injector. The author examined its performance under steady flow with steady voltage, pulsed voltage with steady flow, and pulsed voltage with pulsed flow. With a steady voltage, for a multiple-orifice structure, electrical efficiency increases along with the number of orifices. However, at a high pressure and a jet Reynolds number of about 2000, increasing the number of holes resulted in reducing the spray's specific charge value. For a pulsed voltage, a modified Mitsubishi fuel injector was utilised and a spray's specific charge of 1.4 C/m^3 was obtained.

2.4 Chapter summary

This chapter covers recent scientific progress on droplet vaporisation modelling approaches for biodiesel fuel, and the research carried out up to date in the development of electrostatic atomisers.

Models considering biodiesel fuel as a single element seem to predict evaporation time less accurately than those that focus on its elements. Apart from this, the model's accuracy is also found to be influenced by various correction factors and property-calculation rules.

For modern electrostatic atomisers, the spray-triode concept was a groundbreaking step. Multi-orifice structures are found to have a higher electrical efficiency (the ratio of spray current to total current) than conventional point-plane structures. However, their spray specific charge is lower when compared to single-orifice designs.

3

Methodology

3.1 Introduction

This chapter describes the assumptions, formulation, and solution approach for a single biodiesel droplet-vaporisation model under high-temperature and low-pressure environments. In addition, the breaking up of a charged droplet into a residual droplet and sibling droplets, and their effect on the total vaporisation time, is numerically demonstrated. Details of fuel-property calculations are also provided in this chapter.

3.2 Model formation

To determine the spray quality of a charge-injection atomiser, a fundamental study on droplet evaporation for various operating conditions is necessary. In the case of spray flow with

real engine conditions, interactions are observed between processes such as atomisation, dispersion, and evaporation [34–36]. Thus, creating a model for this complex configuration is always difficult. The other approach is to consider a single isolated droplet, which is undertaken in this thesis. The model is adopted from [37], based on the Langmuir-Knudsen evaporation law for an equilibrium condition. All the governing equations are solved using a 4th-order Runge-Kutta scheme. The number of time steps used is $N_{steps} = 10000$. The MATLAB code is provided in Appendix A. Further details can be found in [38].

3.2.1 Assumptions

To improve our understanding and simplify the model the following assumptions have been made:

- Spherical symmetry is assumed throughout the lifetime of the droplet,
- The liquid density of the droplet is much higher than that of the surrounding ambient gas,
- Momentum transfer with the carrier gas is related only to the drag force,
- The effects of radiation and gravitation are ignored,
- A thermodynamic equilibrium exists between the liquid and gaseous phases at the droplet surface.

3.2.2 The governing equations

For a static suspended droplet, the evaporation rate and the corresponding droplet diameter can be expressed as [37]:

$$\frac{dm_d}{dt} = -\frac{Sh}{3Sc_G} \left(\frac{m_d}{\tau_d} \right) \ln(1 + B_{M,eq}) \quad (3.1)$$

$$D = \left(\frac{24m_d}{4\rho\pi} \right)^{1/3} \quad (3.2)$$

where $m_d = \frac{4}{3}\pi(\frac{D}{2})^3\rho$ is the mass of the droplet, Sh is the Sherwood number which can be defined as the ratio of convective mass transfer to diffusive mass transfer, Sc_G is known as the Schmidt number and is the ratio of momentum diffusivity to mass diffusivity, $\tau_d = \rho_D D^2 / 18\mu_G$, is the droplet relaxation time scale, and $B_{M,eq}$ is the Spalding mass transfer

number for equilibrium conditions given by:

$$B_{M,eq} = \frac{Y_{s,eq} - Y_G}{1 - Y_{s,eq}} \quad (3.3)$$

where $Y_{s,eq}$ and Y_G are the mass fractions in equilibrium conditions at the droplet surface and far from the droplet respectively. $Y_{s,eq}$ can be obtained from:

$$Y_{s,eq} = \frac{X_{s,eq}}{X_{s,eq} + (1 - X_{s,eq})\theta_2} \quad (3.4)$$

where θ_2 is the ratio of the molecular weights and $X_{s,eq}$ is the vapour mole fraction in the equilibrium condition at the droplet surface. It is calculated based on the Clausius-Clapeyron law as follows:

$$X_{s,eq} = \frac{P_{atm}}{P_G} \exp\left[\frac{W_V L_V}{R} \left(\frac{1}{T_B} - \frac{1}{T_D}\right)\right] \quad (3.5)$$

where L_V is the latent heat of vaporisation, W_V is the molecular weight, and R is the universal gas constant. The rate of change of the droplet surface temperature is written as:

$$\frac{dT_d}{dt} = \frac{f_2 N_u}{3 Pr_G} \left(\frac{\theta_1}{\tau_d}\right) (T_G - T_d) + \left(\frac{L_V}{C_L}\right) \frac{\dot{m}_d}{m_d} \quad (3.6)$$

where N_u is the Nusselt number, which is a dimensionless number that indicates the convective to conductive heat transfer normal to the droplet boundary. Pr_G is the Prandtl number and, for a unit Lewis number, $(Sc)_G = (Pr)_G$. θ_1 is the ratio of heat capacities (gas phase to liquid phase), f_2 is the heat-transfer correction caused by evaporation which is equal to 1 for an equilibrium rapid-mixing model and is taken as $f_2 = \beta/e^\beta - 1$ [37] for the model considered in this thesis, where

$$\beta = -\left(\frac{3 Pr_G \tau_D}{2}\right) \frac{\dot{m}_d}{m_d} \quad (3.7)$$

In a quiescent environment, the value for both the dimensionless numbers, Nu and Sh , is equal to 2. However, when taking into account the convection effects, modified empirical correlations [39] are introduced in this approach:

$$Nu = 2 + 0.552 Re_d^{1/2} Pr_G^{1/3} \quad (3.8)$$

$$Sh = 2 + 0.552 Re_d^{1/2} Sc_G^{1/3} \quad (3.9)$$

where Re_d refers to the droplet Reynolds number and is calculated by:

$$Re_d = \frac{\rho D u}{\mu} \quad (3.10)$$

3.2.3 Fuel Properties

The importance of calculating the physical properties of alternative fuels accurately for faithful prediction of spray, atomisation and combustion processes has already been shown in [40, 41]. A list of the effective key parameters involved in the vaporisation process, with their calculating method, is given below:

Density

The following formula [42] is used to determine the density for different FAMES

$$\rho = \rho_o - \alpha(T - 288.15) \quad (3.11)$$

where

$$\rho_o = 851.471 + \frac{250.718 \times DB + 280.899}{1.214 + n_{acid}}$$

and

$$\alpha = \frac{7.536}{\ln(n_{acid}) + 3.584} - 0.446$$

Here, n_{acid} is the number of carbon atoms and DB is the number of double bonds in fatty acids.

Latent heat of evaporation

This is also known as the enthalpy of vaporisation and the higher the value, the more energy does the fuel need to vaporise. It is estimated as [43]:

$$L = (a_L + b_L M)A \quad (3.12)$$

where

$$A = \left(\frac{T_{cr} - T_{avg}}{T_{cr} - T_b} \right)^{0.38} \quad (3.13)$$

and

$$T_{cr} = a_{cr} + b_{cr} M \quad (3.14)$$

$$T_b = a_b + b_b M \quad (3.15)$$

$$T_{avg} = (T_g + T_b)/2 \quad (3.16)$$

where T_{cr} and T_b are the critical and boiling-point temperatures, respectively. T_{avg} is the average of the gas-phase and boiling-point temperatures at the droplet surface.

Liquid heat capacity

To calculate the liquid heat capacity for various temperatures, the formula suggested by Hallett et al. [43] has been used:

$$c = (a_p + b_p T_{avg} + c_p T_{avg}^2) 10^3 \quad (3.17)$$

Vapour heat capacity

With reference to fatty-acid methyl esters, the vapour heat capacity is calculated based on the following equation [24]:

$$C_{fg} = a_{cpv}(T_{avg}/300)^5 + b_{cpv}(T_{avg}/300)^4 + c_{cpv}(T_{avg}/300)^3 + d_{cpv}(T_{avg}/300)^2 + e_{cpv}(T_{avg}/300)^1 + f_{cpv} \quad (3.18)$$

The values of all the coefficients used in (3.11-3.17) are listed in Table 3.1 [44], and for (3.18) the coefficient values can be found in Appendix A7 of [24]. Table 3.2 shows the properties of different fatty-acid methyl esters at different conditions. The expressions for the components represent the number of carbon atoms (n_{acid}) on the left side of ‘:’ and the number of double bonds (DB) on the right side of ‘.’. For instance, C18 : 3 stands for $n_{acid} = 18$ and $DB = 3$.

3.3 Solution approach

In this study, properties are not calculated at every time step, which has already proven computationally expensive for many droplet cases. A different approach is applied, where properties are evaluated based on the estimated average temperature (T_{avg}) at the beginning of each simulation. In a previous study [38], the wet-bulb temperature was used for simpler fuels like decane, hexane, and for water, because of their existing empirical correlations, which are not available for biodiesel fuels. Thus through an assumption, that was suggested by [46], T_{avg} is used in this simulation. This assumption is validated and will be discussed in the model-validation section. Furthermore, it is assumed that the initial droplet temperature

TABLE 3.1: Coefficient values for (3.11-3.17)

Coefficient	C12:0~C24:0	C16:1~C24:1	C18:2	C18:3
a_L	1.506×10^7	1.389×10^7	1.270×10^7	1.154×10^7
b_L	1.814×10^5	1.822×10^5	1.834×10^5	1.843×10^5
a_b	348.7	350.4	352.1	353.82
b_b	0.8478	0.8463	0.8463	0.8472
a_{cr}	534.3	538.5	542.6	546.8
b_{cr}	0.784	0.777	0.772	0.7711
a_p	1.816	1.915	2.018	2.115
b_p	-0.001462	-0.002163	-0.002878	-0.00358
c_p	7.51×10^{-6}	8.29×10^{-6}	9.09×10^{-6}	9.92×10^{-6}

rapidly reaches T_{avg} , and the drop is injected into a pure air environment, which reduces calculations for the mixture. The droplet mass fraction is evaluated based on the instantaneous temperatures, updated in every time step, which in turn reduces the over-prediction of the model. The following are the main steps of the algorithm:

- Depending on the type of methyl esters and ambient temperature, calculate the density, critical and boiling-point temperatures using (3.11), (3.14), and (3.15) respectively.
- Based on the estimated T_{avg} (using (3.16)), calculate the latent heat of evaporation, liquid heat capacity, and vapour heat capacity from (3.12), (3.17), and (3.18) respectively.
- Calculate the vapour molar fraction at equilibrium condition using (3.5).
- Calculate the mass fraction from (3.4) and use it to determine the Spalding mass transfer number using (3.3).
- Calculate the empirical correlations Nu and Sh from (3.8) and (3.9), respectively.
- Calculate the evaporation rate using (3.1).
- Calculate successive reductions in droplet diameter in accordance with the mass of the droplet from (3.2).
- Calculate the rate of change of the droplet temperature using (3.6).
- Repeat from step one until the mass of the droplet is reduced to 0.1% of the original mass.

TABLE 3.2: Properties of FAMEs
FAME

Properties	C12:0	C14:0	C16:0	C16:1	C18:0	C18:1	C18:2	C18:3
Chemical formula	$C_{13}H_{26}O_2$	$C_{15}H_{30}O_2$	$C_{17}H_{34}O_2$	$C_{17}H_{32}O_2$	$C_{19}H_{38}O_2$	$C_{19}H_{36}O_2$	$C_{19}H_{34}O_2$	$C_{19}H_{32}O_2$
Name	Methyl	Methyl	Methyl	Methyl	Methyl	Methyl	Methyl	Methyl
	dodecanoate	tetradecanoate	palmitate	palmitoleate	stearate	oleate	linoleate	linolenate
Molecular weight	214.338	242.39	270.442	268.426	298.494	296.478	294.462	292.446
(kg/kmol)[24]								
Density at 25°C	847.8	847.9	848.1	847.6	848.2	848.4	847.9	848.1
(kg/m ³)[24]								
Boiling point(°C)	257.4	281.2	305	304.56	329.76	328.31	328.33	328.58
at 1 atm[44]								
Liquid heat capacity at 25°C	2498.5	2556.1	2615.9	2556.9	2680.4	2618.5	2561.8	2511.7
(J/kgK)[44]								
Flame temperature (K)[45]	2450	2500	2525	2525	2540	2540	2540	2540

3.4 Evaporation of charged droplet

3.4.1 Charge-only case

The model is also used to predict the total vaporisation time for charged droplets of individual FAMES by modifying the droplet diameter when it reaches the Rayleigh limit. In a charge-injection atomiser, the surface energy which promotes atomisation is obtained from the mutual repulsion of the net charges which accumulate on the whole or partial surface of the droplets, and a single droplet with a diameter D [m] can hold a maximum surface charge given by [38]:

$$Q_{ray} = \pi(\varepsilon\sigma)^{1/2}(2D)^{3/2} \quad (3.19)$$

where ε is the permittivity of vacuum [F/m], σ is the surface tension [N/m] and (3.19) is known as the Rayleigh limit. Through the vaporisation process, the droplet diameter decreases, and as its charge (Q_O) approaches the Rayleigh limit fragmentation occurs. The core droplet separates into a larger residual droplet and into n smaller sibling droplets. Fig.3.1 depicts the typical fragmentation process of a charged droplet and the gradual reduction of the residual droplet diameter.

In practice, individually charged droplets usually break up well below the Rayleigh limit

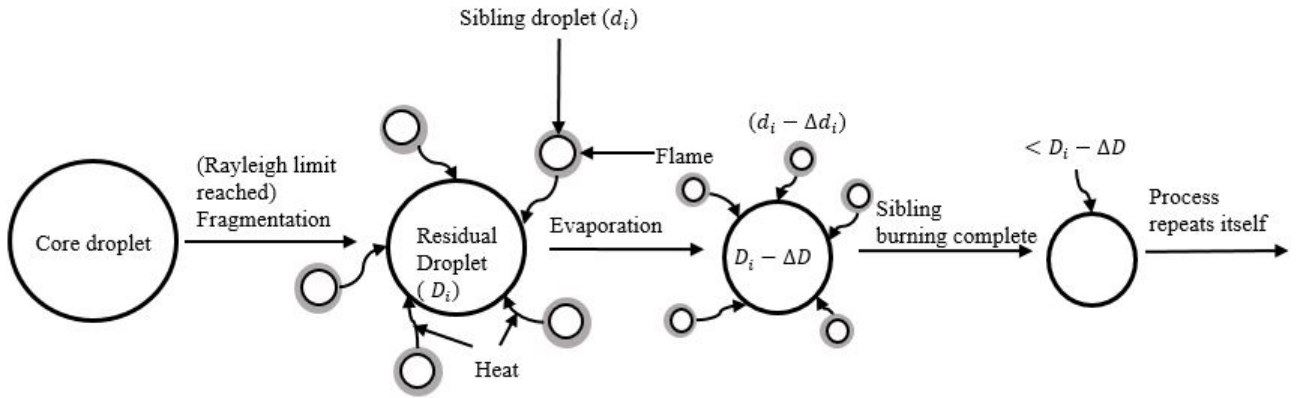


FIGURE 3.1: Schematic of a charged droplet fragmentation, evaporation, and combustion process.

[18] and therefore the fragmentation limit can be rewritten as follows:

$$Q_{ray} = \eta\pi(\varepsilon\sigma)^{1/2}(2D)^{3/2} \quad (3.20)$$

where η is the Rayleigh limit coefficient ($\eta \leq 1$), typically equal to 0.8 in this thesis unless otherwise specified. Based on previous studies [38], for the whole simulation, it is assumed that, after fragmentation, the residual droplet has a mass (m_1) of 97.5% of the mass (m_o) of the core droplet and a charge (Q_{res}) of 80% of the charge of the core droplet (Q_o). The remainder of the mass is distributed among the siblings and, depending on the number of siblings (n), the mass carried by an individual sibling can be calculated from (3.21). For this study, it is assumed that $n = 5$.

$$m_{sib} = \frac{(1 - 0.975) \times \text{mass of the core droplet}}{\text{number of siblings}(n)} \quad (3.21)$$

3.4.2 Charge and combustion case

During combustion, the sibling droplets are assumed to be enveloped by individual flames at the adiabatic flame temperature as shown in Fig.3.1, and burn according to a D^2 law. Therefore, the evaporation time for the siblings is calculated as:

$$t_{evap} = \frac{d^2}{k} \quad (3.22)$$

where

$$k = \frac{8k_g}{\rho_d C_{p,g}} \ln(1 + B_q)$$

d is the diameter of the siblings [m], k is the evaporation constant [m^2/s], k_g is the thermal conductivity of the gas [W/(m K)], ρ_d is the density of the liquid [kg/m^3], $C_{p,g}$ is the gas-phase specific heat capacity [J/(kg K)], and B_q is the Spalding heat-transfer number which is estimated as:

$$B_q = \frac{\Delta h_c / v_{a,f} + C_{p,g}(T_g - T_b)}{L_v}$$

where Δh_c is the combustion heat and $v_{a,f}$ is the stoichiometric air-fuel ratio. The residual droplet's vaporisation time is influenced by the combustion heat generated during the sibling's burning throughout its lifetime and is calculated as [38]:

$$\frac{dT_d}{dt} = \frac{f_2 N_u}{3 P_{rG}} \left(\frac{\theta_1}{\tau_d} \right) \left(\left(\frac{T_G + T_F}{2} \right) - T_d \right) + \left(\frac{L_V}{C_L} \right) \frac{\dot{m}_d}{m_d} \quad (3.23)$$

Fig. 3.2 shows the numerical process of taking into account sibling droplet combustion and its influence on total vaporisation. In this modelling approach, cyclic fragmentation of the siblings generated from the core droplet into further siblings is not accounted for [38].

3.5 Chapter summary

This chapter statistically describes the necessary assumptions and equations required to model the vaporisation process for a biodiesel droplet having electrostatic charge on its surface. In this approach the convective effect is considered through Nusselt-number and Sherwood-number corrections. The properties of individual FAMEs are also evaluated and listed in this chapter.

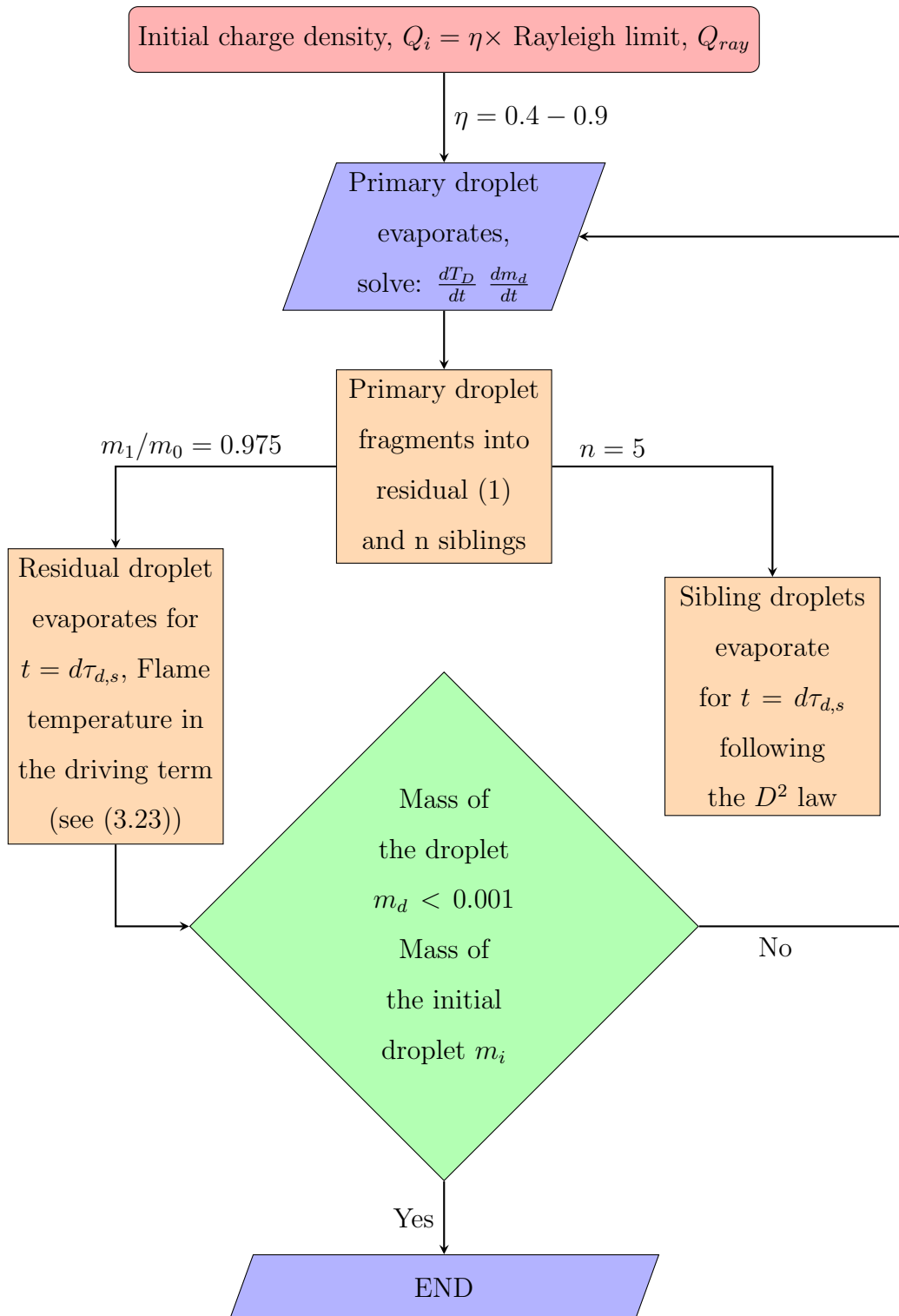


FIGURE 3.2: Flowchart showing the steps of fragmentation of a core droplet into a residual and n siblings and their contribution towards the droplet vaporisation.

4

Results and Discussion

4.1 Introduction

The overall aim of this chapter is to present and analyse the results. Initially, the model is validated with experimental results. Following this the predictions for an individual FAME charged droplet as functions of various critical parameters are examined.

4.2 Model validation

The validation of this model has already been conducted in a previous study [38] with iso-octane for the electrical charge and a sibling's combustion, and with simple fuels such as decane and hexane, and water, for the no-electrical-charge case. In this study, the performance of this model with single-component FAMEs is evaluated by comparing its predictions

to one of the experimental results [20] which consisted predominantly of C16:0, as shown in Fig.4.1 (for the case of no electrical charge) thereby leading to excellent agreement with the model. The initial increment in droplet diameter for the experimental case is a result of thermal expansion, which is not considered in the current modelling approach. The maximum deviation (13.6%) for computing the total evaporation time shows up for C12:0, which is the minimal portion of the fuel (sample 1) that was used in experimentation. Further validation of the evaporation model may be found with simpler fuels in [38].

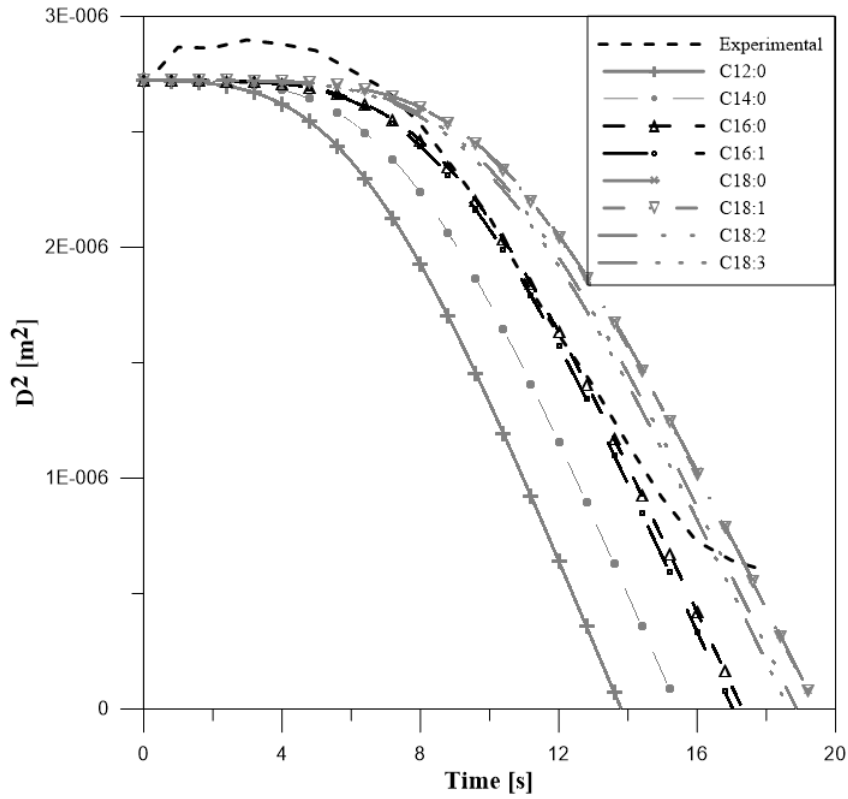


FIGURE 4.1: Comparison between the predictions of the present model and experimental findings for the D^2 versus time history of FAMEs. Initial conditions are: $T_g = 420$ °C, $D = 1.62$ mm, $T_d = 25$ K, $R_e = 0$, and $P_\infty = 1$ atm.

4.3 Model predictions

Fig.4.2 shows the evaporation history of a stagnant Stearate (C18:0) droplet for three cases: (i) evaporation without charge; (ii) evaporation with charge; and (iii) evaporation with charge and combustion. The objective of this figure is to illustrate the effect of charge and

sibling combustion in the evaporation-time calculation, which is clearly visible. The droplet fragmentation and sibling contribution follow the process shown in Fig.3.2 and explained in Section 3.4.2 in the previous chapter.

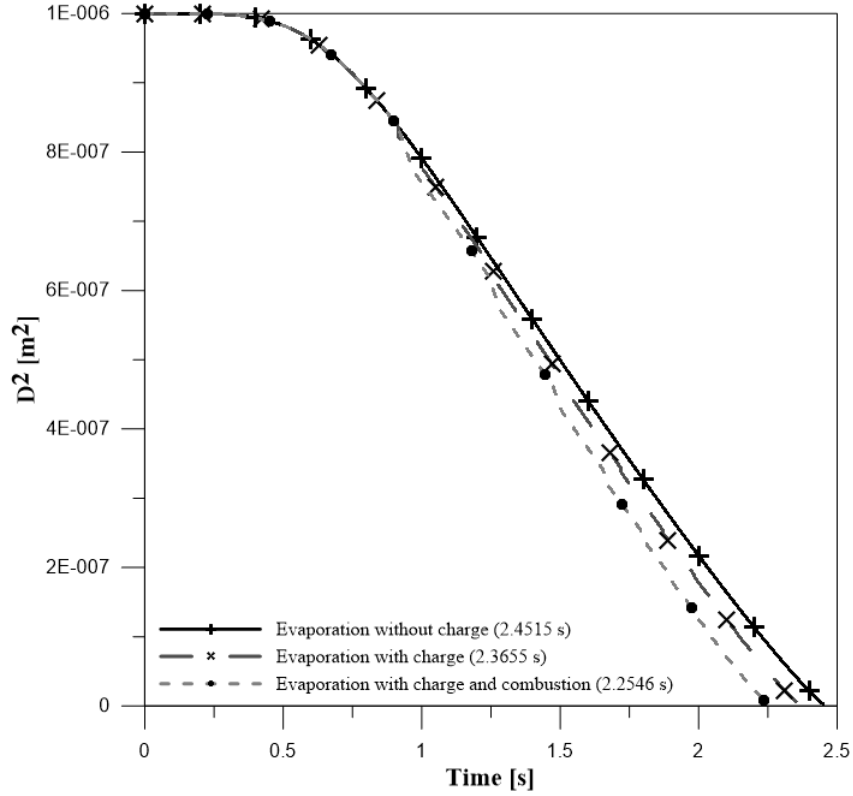


FIGURE 4.2: D^2 history for a Stearate (C18:0) droplet with no charge, with charge and no reaction, and with charge and reaction for $n = 5$; Initial conditions are: $D = 0.001$ m, $T_g = 600$ K, $T_d = 298$ K, $R_e = 0$, and $Q_i/Q_{ray} = 0.7$.

4.3.1 Effect of initial charge density

The initial charge (Q_i) on the droplet as a function of the Rayleigh limit, Q_{ray} , is an important key parameter with experimental relevance. The response of all the FAMEs has been tested with respect to initial charge densities varying from $Q_i/Q_{ray} = 0.4 - 0.9$ in increments of 0.1. Regardless of the ambient temperature and for any of the methyl esters, the same trend is observed, and thus the result only for C18 : 0 is shown in Fig.4.3. On the y axis, Δt represents the vaporisation time difference for the following cases: (i) a core droplet and a core droplet with charge; and (ii) a core droplet and a core droplet with charge and sibling

droplet combustion. Throughout this chapter Δt will have the same meaning, and cases (i), and (ii) will be noted as the charged case and the charge+combustion cases respectively. From Fig. 4.3 it is clear that the effect of charge increases with increasing initial charge density for the considered range, with a significant impact up until $(Q_i/Q_{ray} = 0.7)$. Above that level the effect of charge diminishes due to the fixed Rayleigh limit coefficient, $\eta = 0.8$, which has been adopted. This makes the Rayleigh limit coefficient an important parameter to determine when designing an electrostatic atomiser.

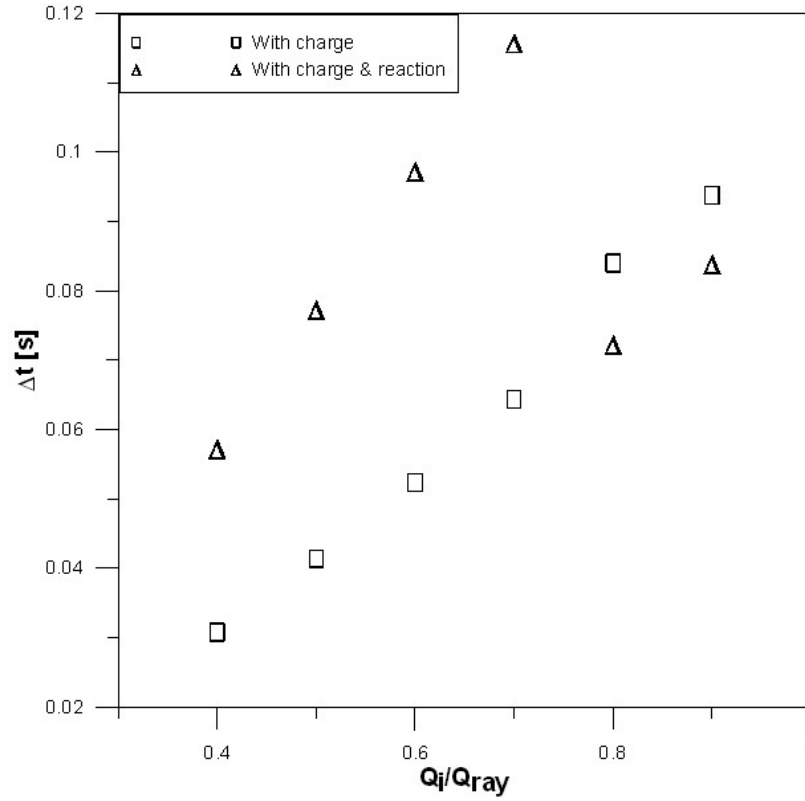


FIGURE 4.3: Vaporisation time difference versus initial charge density factor (Q_i/Q_{ray}) for charge and reaction cases with $n = 5$. Initial conditions are: $D = 0.001$ m, $T_g = 700$ K, $T_d = 298$ K, and $R_e = 0$.

4.3.2 Effect of ambient temperature

Evaporation with charge:

The amount of charge injected by an electrostatic atomiser per unit time is referred to as the total current, which is a combination of leakage current (lost to ground) and spray current

(carried out by the liquid into the spray). The performance of an atomiser is assessed by measuring its spray current because the higher the spray current, the better the atomisation. Fig.4.4 shows the effect of charge on FAMEs for the chosen range of temperatures. The maximum vaporisation time difference is observed for C18:0; it is a minimum for C12:0. According to Shrimpton [9], for a highly viscous fluid the residence time of an ion increases, resulting in an increase in the spray current with respect to the leakage current. For FAMEs, increasing the chain length coincides with an increase in viscosity. However, a higher degree of unsaturation also reduces the viscosity, and this effect is apparent for C18:2 and C18:3 in Fig.4.4. The effect of charge decreases for all FAMEs with increasing ambient temperature. At 800 K, the effect is at its minimum and is similar for all the FAMEs, which can be explained using a mass-fraction contribution as follows.

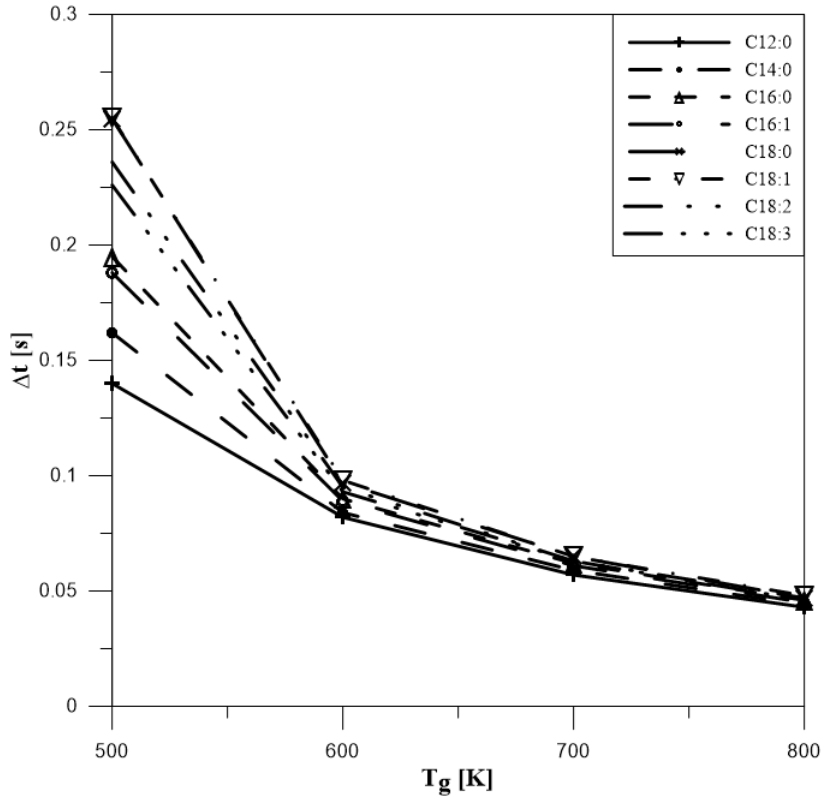


FIGURE 4.4: Vaporisation time difference versus ambient temperature for various FAMEs with no-charge and charge cases. Initial conditions are: $D = 0.001$ m, $T_d = 298$ K, $R_e = 0$, and $Q_i/Q_{ray} = 0.7$.

From (3.1) and (3.3), it is clear that the evaporation rate is strongly related to the mass fraction. As the ambient temperature increases, the mass fraction of the vapour at the

droplet surface, regardless of having charge or not, also increases as shown in Fig.4.5. At high temperatures, for all the FAMEs, the value becomes similar for all the fuels, therefore predicting almost identical evaporation times for both conditions, i.e. a droplet with and without charge. This suggests that the influence of charge in cold conditions may be more beneficial, which from a practical point of view would occur in the near field of the spray.

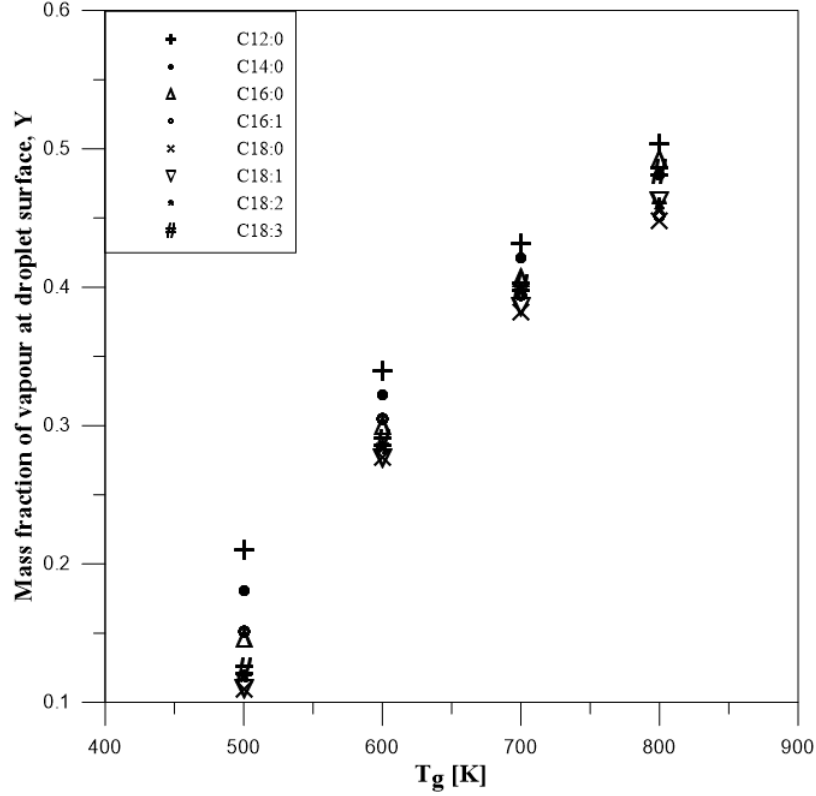


FIGURE 4.5: Mass fraction of the vapour at droplet surface versus ambient temperature for all the FAMEs. Initial conditions are: $D = 0.001$ m, $T_d = 298$ K, $Re = 0$, and $Q_i/Q_{ray} = 0.7$.

Evaporation with charge and combustion:

The amount of heat generated from the combustion of siblings influences the vaporisation time of the residual droplets and contributes to reducing the overall evaporation time further. Fig.4.6 shows the effects of charge and combustion as a function of ambient temperature (T_g) for all the FAMEs. A reduction in sensitivity is again observed with increasing T_g . However, at 800 K a variation is noted. Linoleanate ($C18 : 3$), although it was more sensitive than Palmitate ($C16 : 0$) at 500 K, throughout the temperature range loses its sensitivity, and at 800 K, $C16 : 0$ becomes more sensitive to charge regardless of having a shorter carbon chain.

This statement is found to be valid for predicting their lifetime as well. A higher value of the evaporation constant (k) would possibly be responsible for this step down for $C18 : 3$. As observed by Hashimoto et al. [47], the evaporation constant (k) increases with increasing T_g , and the higher value of k predicts a shorter lifetime. Fig.4.7 makes it clear that at 800 K, the value of k is higher for $C18 : 3$ than for $C16 : 0$, which likely causes this variation. However, this trend is not reflected by all the FAMEs here, as siblings carry only 2.5% of the mass of the total core droplet.

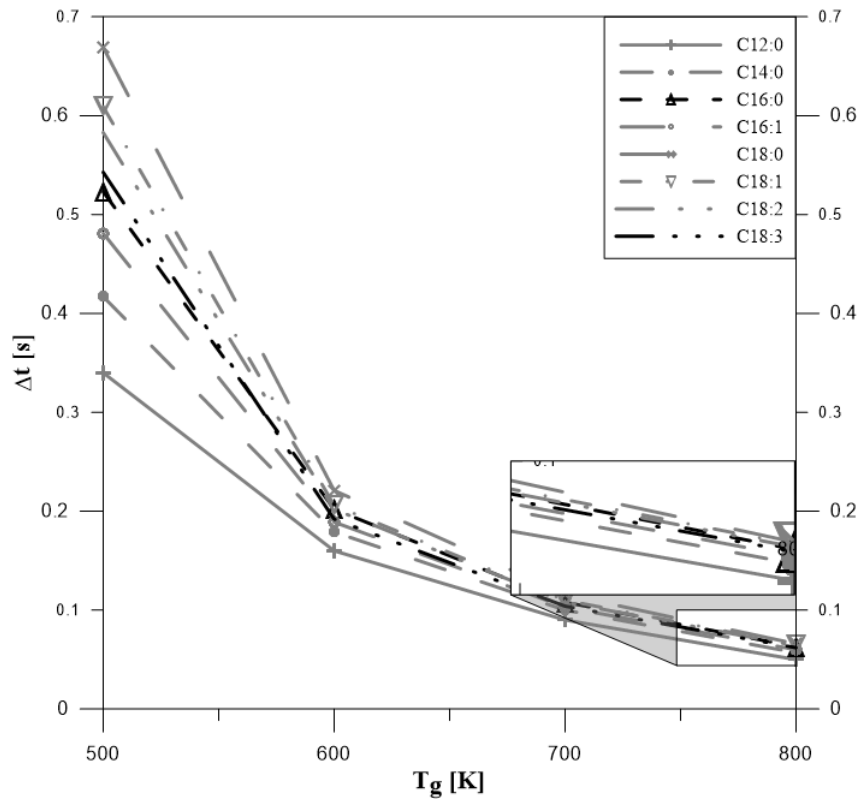


FIGURE 4.6: Vaporisation time difference versus ambient temperature with charge and reaction cases for $n = 5$. Initial conditions are: $D = 0.001$ m, $T_d = 298$ K, $R_e = 0$, and $Q_i/Q_{ray} = 0.7$.

4.3.3 Effect of Reynolds number

To predict the vaporisation time of droplets for given operating conditions and fuel properties, the droplet Reynolds number is of great importance. Fig.4.8 shows the effect of the droplet Reynolds number on the calculated evaporation time difference for both cases. Here, the result for only $C18 : 0$ is presented, since the other fuels follow the same pattern. It

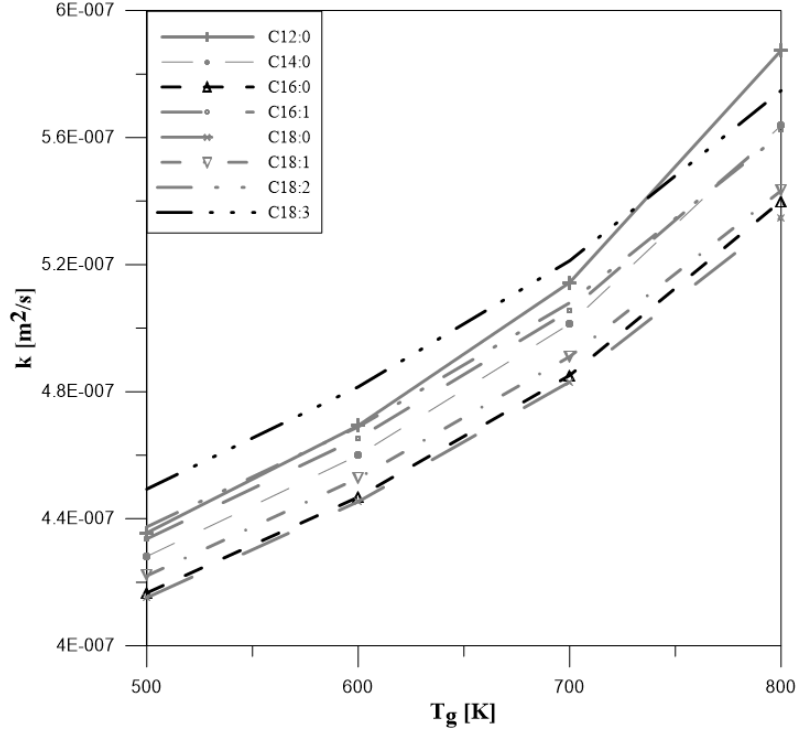


FIGURE 4.7: Evaporation constant versus ambient temperature for various FAMEs with no charge. Initial conditions are: $D = 0.001$ m, $T_d = 298$ K, $Re = 0$, and $Q_i/Q_{ray} = 0.7$.

is clear that the effect of charge on the total vaporisation time decreases with increasing Re while, taking into account the siblings' combustion, the effect increases with increasing Re . This outcome agrees with previous work carried out with simpler fuels [38]. In general higher Reynolds number predicts less evaporation time whether the droplet has a charge or otherwise. However, referring to the combustion case, the generated heat resulting from siblings burning pulls the vaporisation time-difference curve upward.

4.4 Chapter summary

This chapter has presented the validation of the model and its ensuing predictions. The vaporisation results for charged FAME droplets are analysed under experimentally relevant operating conditions such as initial charge density, ambient temperature, and droplet Reynolds number. The effect of charge is found to increase proportionally with the initial charge

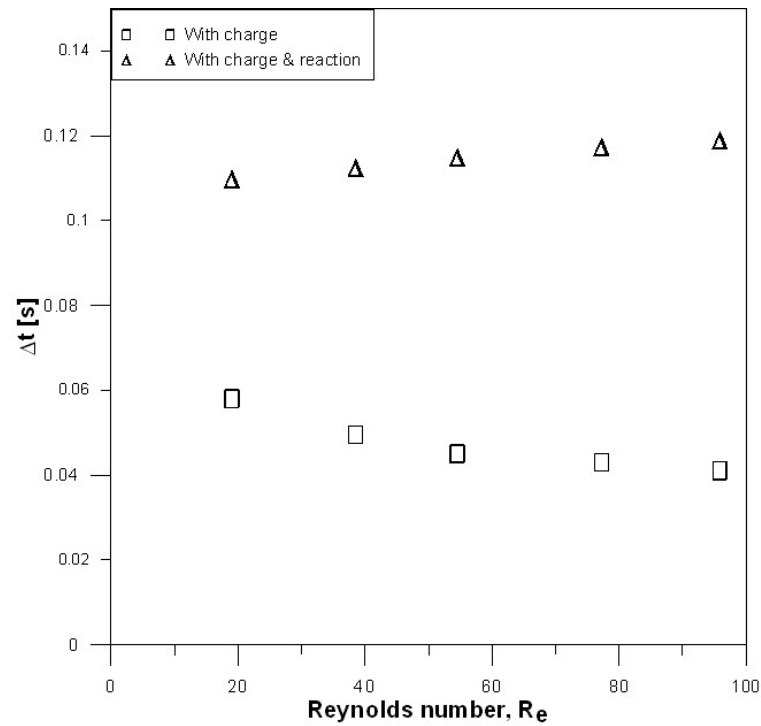


FIGURE 4.8: Vaporisation time difference versus Reynolds number with charge and reaction cases for $n = 5$. Initial conditions are: $D = 0.001$ m, $T_d = 298$ K and $Q_i/Q_{ray} = 0.7$

density, while an increase in ambient temperature resulted in reducing the effect. Droplet Reynolds number shows a mixed effect for the cases considered here. Finally, throughout the analysis, C18:0 appears to be more sensitive to the charge compared to all the other FAMES.

5

EHD flow inside the atomiser

5.1 Introduction

This chapter focuses on the transportation of charge from the emitter electrode to the insulating liquid. This charge ultimately advects out to the atomiser through electrohydrodynamic (EHD) means and influences the atomisation and evaporation process (which has been described in the previous chapter). EHD is governed by various dimensionless numbers which will be discussed here; data from direct numerical simulation is analysed to gain further insight into EHD flow and the distribution of charge with respect to the bulk-flow velocity and dimensionless numbers of practical relevance.

5.2 Theoretical study

Electrohydrodynamics (EHD) is an interdisciplinary area which deals with the interaction between hydrodynamic and electrical forces. In a charge-injection atomiser as shown in Fig.5.1, the generated electrical field (acting across the gap of thickness d), due to the applied electrical potential, starts driving the charges away from the emitter. The Coulomb force pushes these space charges along with the liquid and, if the potential is high enough, instability is formed. The liquid present between the electrodes starts moving with a roll-like structure [48, 49] as shown in Fig.5.2, and the distribution of the charge within the liquid is related to this flow pattern. Thus, to improve the performance of a charge-injection atomiser, it is necessary to understand the underlying physics of these EHD instabilities.

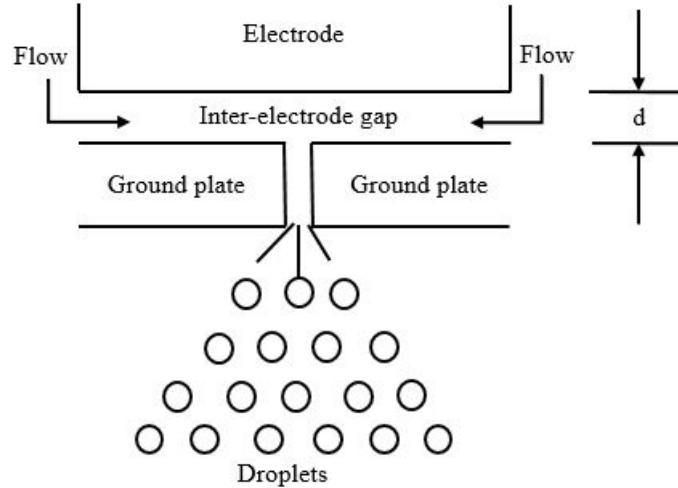


FIGURE 5.1: Schematic of a typical electrostatic atomiser.

In this study, a charge-injection process for a simple 2D Poiseuille flow is analysed. For the sake of simplicity, the internal geometry of a typical electrostatic atomiser is considered as a system of two parallel plates of length l , immersed in an insulating liquid and placed at a distance d . Unipolar charge injection is assumed. An electrical potential (V) is applied between the plates to initiate the charge-injection process. The charge carriers are considered to be of the same type, with an ionic mobility k , so they move toward the collector with an ionic drift velocity kE , where E is the generated electrical field.

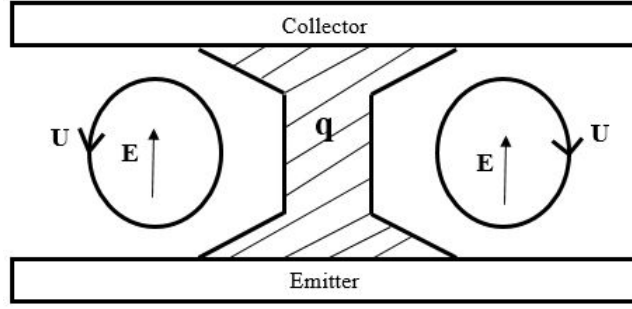


FIGURE 5.2: Typical flow pattern of insulating liquid through two parallel plates.

5.3 Governing equations

Castellanos [48] explained the motion of this charged insulating liquid by simplifying the Maxwell equations. The author used various scales, non-dimensional numbers, and assumed that the electrical energy $((1/2) \varepsilon E^2)$ is greater than the magnetic energy $(B^2/2\psi)$ so that the system is electric-field dominated. Here ε is the permittivity, ψ is the permeability, and B is the magnetic field. This assumption eliminates all the electromagnetic terms and radioactive effects. Therefore, mathematically the assumption is only valid when

$$\frac{1/2 \nabla E^2}{B^2/2\psi} = \frac{E^2}{c^2 B^2} \gg 1 \quad (5.1)$$

Thus, the Maxwell equations for charge injection into an insulating liquid can be reduced to the following:

$$\nabla \times E = 0 \quad (5.2)$$

$$\nabla \cdot E = \frac{q}{\varepsilon} \quad (5.3)$$

$$\frac{\partial q}{\partial t} + \nabla \cdot J = 0 \quad (5.4)$$

The instantaneous continuity equation for a constant-density fluid remains the same regardless of any electrical charge present. The Navier-Stokes equation for the conservation of mass and momentum becomes:

$$\nabla \cdot u = 0 \quad (5.5)$$

$$\rho \left[\frac{\partial u}{\partial t} + u \cdot \nabla u \right] = - \nabla p + \mu \nabla^2 u + \rho g + f \quad (5.6)$$

where u is the injection velocity; p is the pressure; g is the acceleration due to gravity and f is the electrical force, which can be given as:

$$f = qE - \frac{E^2}{2} \nabla \varepsilon + \nabla \left[\frac{E^2}{2} \rho \frac{\partial \varepsilon}{\partial \rho} \right] \quad (5.7)$$

The first expression from the left is the Coulomb (or Lorentz) force term which is the only one relevant for this study. The second expression is known as the dielectric force and is applicable when the system is dealing with alternating current. The final expression refers to the electrostrictive pressure. Considering the constant variation of permittivity in all directions, $\Delta \varepsilon = 0$, (5.6) can be written below as:

$$\rho \left[\frac{\partial u}{\partial t} + u \cdot \nabla u \right] = - \nabla p + \mu \nabla^2 u + \rho g + qE \quad (5.8)$$

where qE is the perturbation of force which generates a small velocity perturbation u , and the system stability largely depends on the coupling of these perturbations. If u destroys this charge-density perturbation, the system will experience a negative coupling and become stable. On the other hand, in the case of positive coupling, the increased value of q will contribute to further charge-density perturbation and the system will become unstable. Based on the Rayleigh-Bénard problem, fluid viscosity also plays a vital role in such a situation since viscosity always delays the onset of motion. Thus the movement of this charged insulating liquid depends on balancing these two force terms, and that gives the first non-dimensional parameter (T) as:

$$T = \frac{\text{Coulomb force}}{\text{Viscous force}} = \frac{qE}{(\mu u)/d^2} \quad (5.9)$$

where u is the characteristic velocity. Based on Poisson's equation $qE = (\epsilon V^2)/d^3$, (5.9) can be rewritten as:

$$T = \frac{\varepsilon V}{k\mu} \quad (5.10)$$

The value of T at which the instability starts is known as the critical stability parameter, and is denoted as T_c .

Now, depending on the velocities, the velocity of the fluid (u) and the velocity of the charge carriers with respect to the fluid (u_c), if either $u \ll u_c$ or $u \gg u_c$, the effect of this

fluid motion in the transportation of charge to the collector varies [49]. To get an idea about the value of u , let us consider that there is a conservation of electrostatic energy to kinetic energy [49]:

$$\begin{aligned}(\varepsilon E^2)/2 &\sim (\rho u^2)/2 \\ u &\sim \sqrt{\varepsilon/\rho} E \\ u &\sim k_H E\end{aligned}$$

where k_H is known as the hydrodynamic mobility and leads to a second non-dimensional parameter M as

$$M = \frac{k_H}{k} = (\sqrt{\varepsilon/\rho})/k \quad (5.11)$$

A higher value of M indicates a larger transformation of electrical energy to kinetic energy. For stability analysis, there is no effect of M [49].

The third non-dimensional parameter is C , which can be defined as the ratio of ionic drift to space-charge relaxation and is used to define the injection strength.

$$C = \frac{qd^2}{\varepsilon V} \quad (5.12)$$

The injection is referred to as strong or weak for values of C in the order of $C \gg 1$ and $C \ll 1$ respectively. In the case of strong injection, the electric field is influenced by the space-charge distribution, while for weak injection the electric field is the supply voltage itself.

An electrical Reynolds number (R_{eE}), which is similar to the conventional Reynolds number (R_e), is also used to explain the charge-injection process at the inter-electrode gap. R_{eE} is defined as the ratio of the inertia force due to ionic drift to the viscous force and can be given by:

$$Re_E = \frac{\rho(kE)d}{\mu} \quad (5.13)$$

These non-dimensional numbers have been calculated previously for charge-injection systems. The critical stability parameter is found as $T_c = 160$ and $T_c = 23450$ for strong

($C = 10$) and weak ($C = 0.1$) injection, respectively [50, 51]. Apart from this, the data on injection strength suggests that most of the atomisers work within a range of $1 \leq C \leq 10$ [52]. As well, experimentally, the electrical Reynolds number (R_{eE}) varies from 10^{-2} to 1 [50]. Thus, to examine the effect of EHD instabilities on the charge distribution across the domain, a typical layout of a charge-injection atomiser is studied by taking $C = 10$ and $R_{eE} = 1$, where T is varied from 500 to 3000.

5.4 Charge distribution analysis

Existing data from a direct numerical simulation (DNS) is utilised to look into the flow pattern between the electrodes and is post-processed to get an insight of instabilities and their effects on the charge distribution. The boundary conditions and solution domain are shown in Fig.5.3. A second-order implicit-finite-volume scheme (QUICK scheme) was employed to solve the charge transportation and momentum equations. A non-uniform grid with 80×80 control volumes was adopted to resolve the flow and the time step was taken as 0.01 s. Due to page limitation, further details such as validation of this simulation and justification of the charge-injection boundary condition are not explained here, which can be found in [53]. The data processing codes for Fig.5.5 and Fig.5.6 are given in Appendix B.

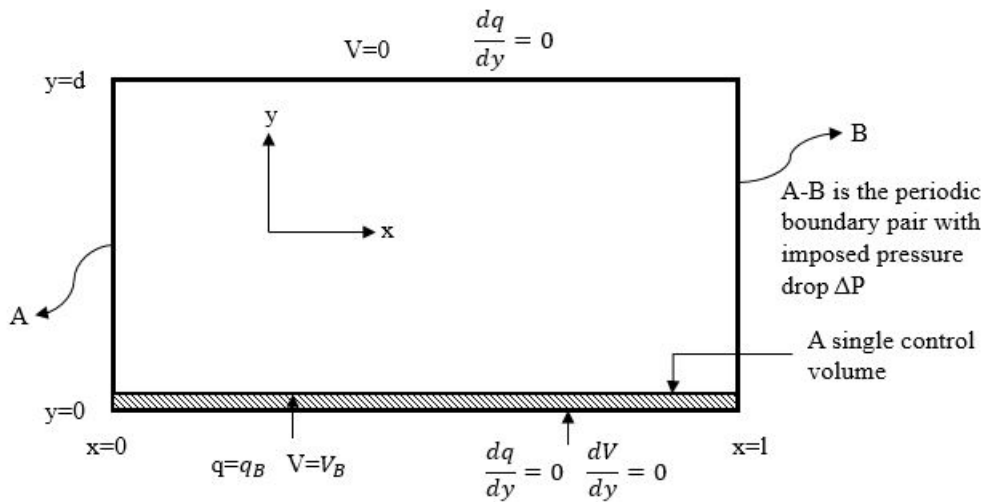


FIGURE 5.3: Boundary conditions and solution domain.

5.4.1 Effect of electrical Rayleigh number (T)

Fig.5.4 shows the contours of the normalised space charge distribution. At $T = 500$, standard double-roll structures appear, which was also previously observed by [54]. The sliding of these stable rolls starts at around $T = 750$. For the cases of $T = 1500$ and $T = 3000$, stretching of these rolls is clearly visible in Figs.5.4(g)-(i). As a result of roll stretching, the space charge seems to be advected to the next roll. This phenomenon is clearer in Fig.5.3(i), where the charge is stripped away from one roll to the next one, lowering the degree of charge stratification in the middle of the domain.

5.4.2 Effect of average bulk-flow velocity (U_{av})

The average bulk-flow velocity (U_{av}) generated from the pressure drop between A and B (as shown in Fig.5.3) is scaled as $U_{av} = kE$, given that significant instability starts only when the ionic drift velocity attains the same order as the bulk-flow velocity of the liquid. From Figs.5.4(a)-(d), it is clear that, for a particular value of T , the standard double-roll structures tend to become unstable with an increase in U_{av} . When the value of U_{av} become significantly high, it destroys all the instabilities and the flow stabilises as shown in Fig.5.4(d). In the context of a charge-injection atomiser, in this situation, all the charges will be swept away outside the atomiser. In other cases ($T = 750, T = 1500$, and $T = 3000$), the same trend with increasing U_{av} is evident.

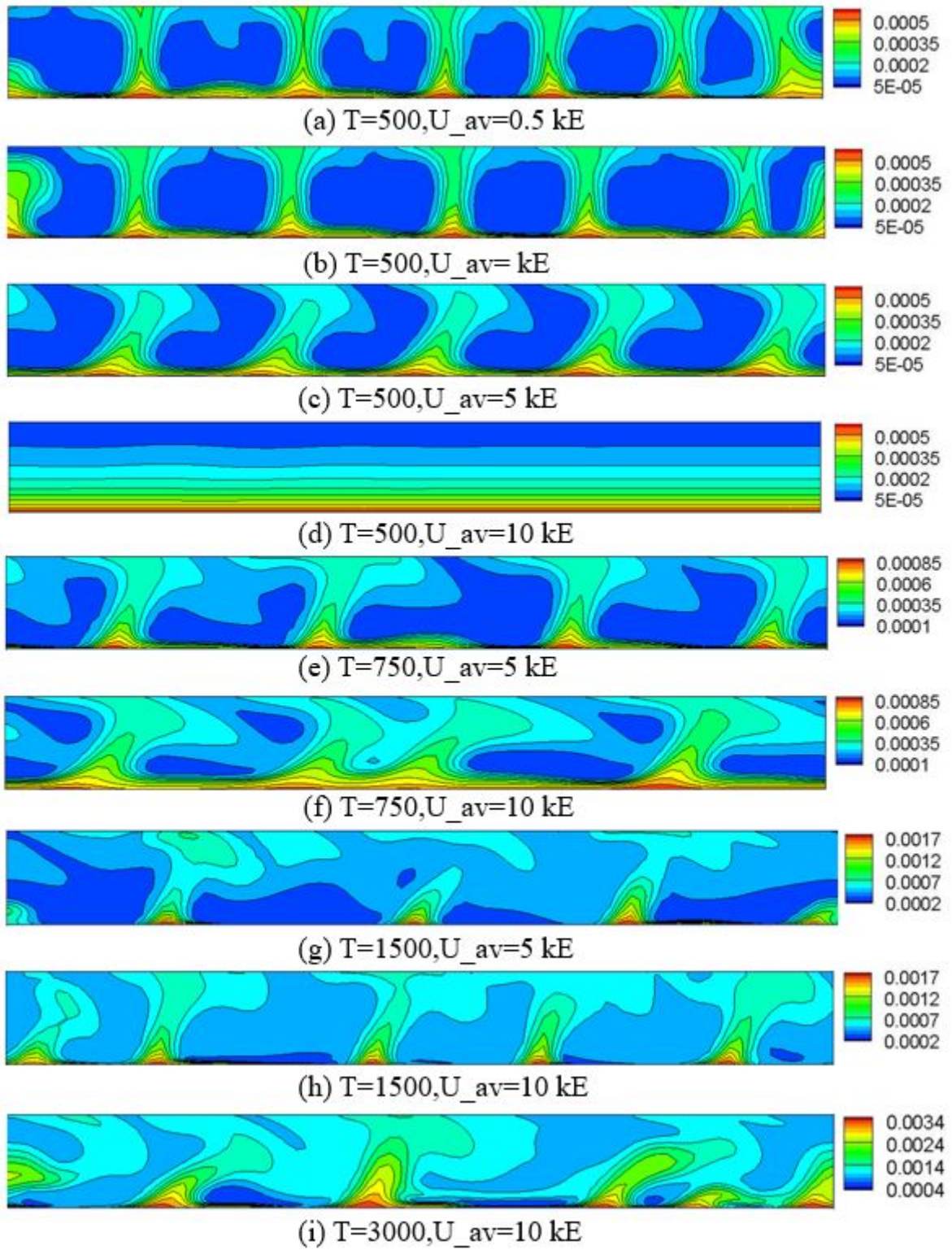
Fig.5.5 shows the normalised time-averaged space-charge distribution as a function of (y/d) along with the analytical solution for charge injection with no bulk convection. The distance $y/d = 0$ refers to the location of the emitter electrode and $y/d = 1$ for the collector electrode. From Fig. 5.5, it is clear that very close to the emitter electrode, at about $y/d = 0.1$, regardless of the conditions, the charge decay is identical for all the considered cases. This suggests that the sudden charge drop near the emitter, even with a high-flow-rate atomiser, is unavoidable. On the other side, near the collecting electrode, higher T is found to predict a higher amount of charge, which seems to be stepped down along with increasing the bulk-flow velocity (U_{av}) for that particular electrical Rayleigh number. In the context of a charge injection atomiser, this finding suggests that the charge drain is higher for the cases

having greater instabilities in their flow while the higher flow rate can reduce these leakage currents.

Fig.5.6 illustrates the spatially averaged space charge at $y = 0.5d$. This investigation is done to see for which cases the charge in the middle of the domain is higher. The oscillations in the line represent the existence of rolls. Despite higher leakage current as previously observed, $T=3000$ drops the maximum amount of charge in the middle of the domain as well. In addition, as found in contour plots (Figs.5.4(a)-(d)), the effect of U_{av} for a particular T value is can be clearly seen in Fig.5.6. Along with an increasing value of U_{av} , the graph tends to smooth, and at a sufficiently higher value becomes plain as reflected for $T = 500, U_{av} = 10kE$. In this case, the existing charge between the electrodes is due to pure charge injection with no convection. The picture of a pure charge injection can be seen in Fig.5.4 (d) while the case involving combination with convection is in Fig.5.4 (c).

5.5 Chapter summary

This chapter has reviewed the EHD governing equations and describes the dimensionless parameters. The DNS data are post-processed to observe the charge distribution throughout the domain with varying electrical Rayleigh numbers and bulk-flow velocities. In the range that has been considered, $T = 3000$ is found to be more effective in moving the charges away from the emitter electrode. In a real charge-injection system, this T value can be achieved by adjusting the voltage and charge level. In addition, the higher value of U_{av} is found to play an important role in reducing the charge transfer to the collector electrode. It can therefore be concluded that in a high-flow-rate atomiser, higher instabilities will increase the overall efficiency.

FIGURE 5.4: Normalised space-charge distribution as a function of T and U_{av}/kE .

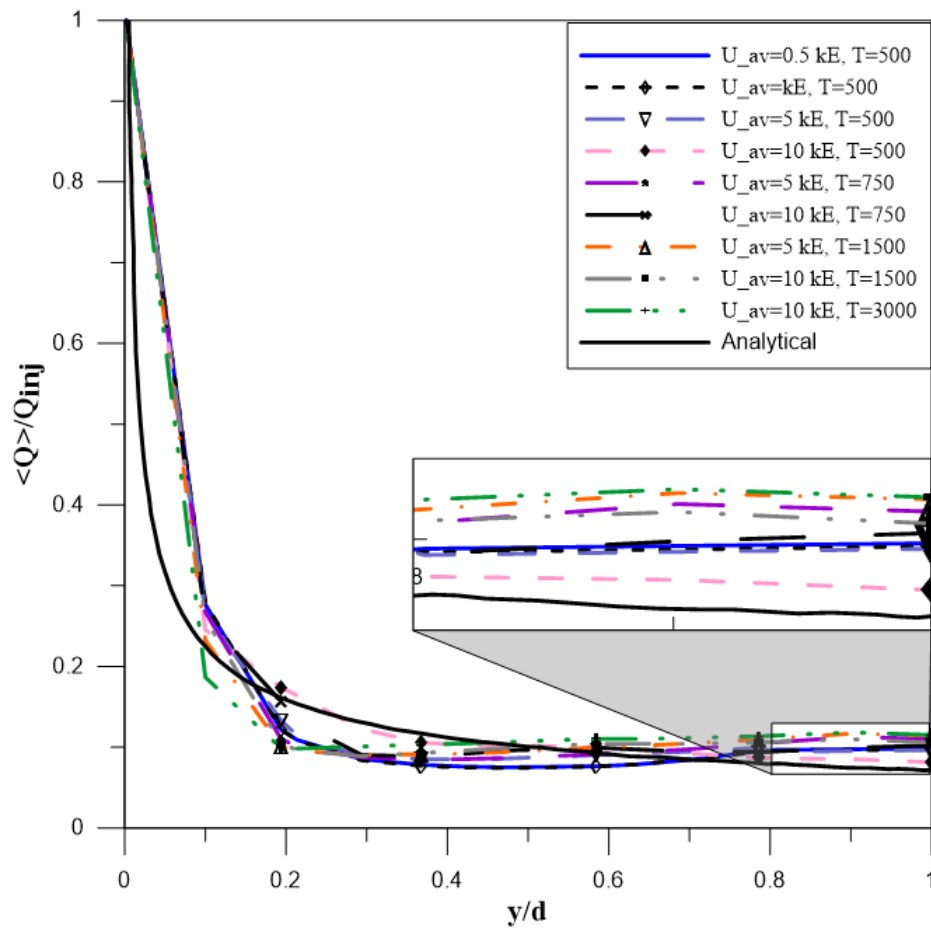


FIGURE 5.5: Distribution of normalised space charge in vertical locations as a function of T and U_{av}/kE .

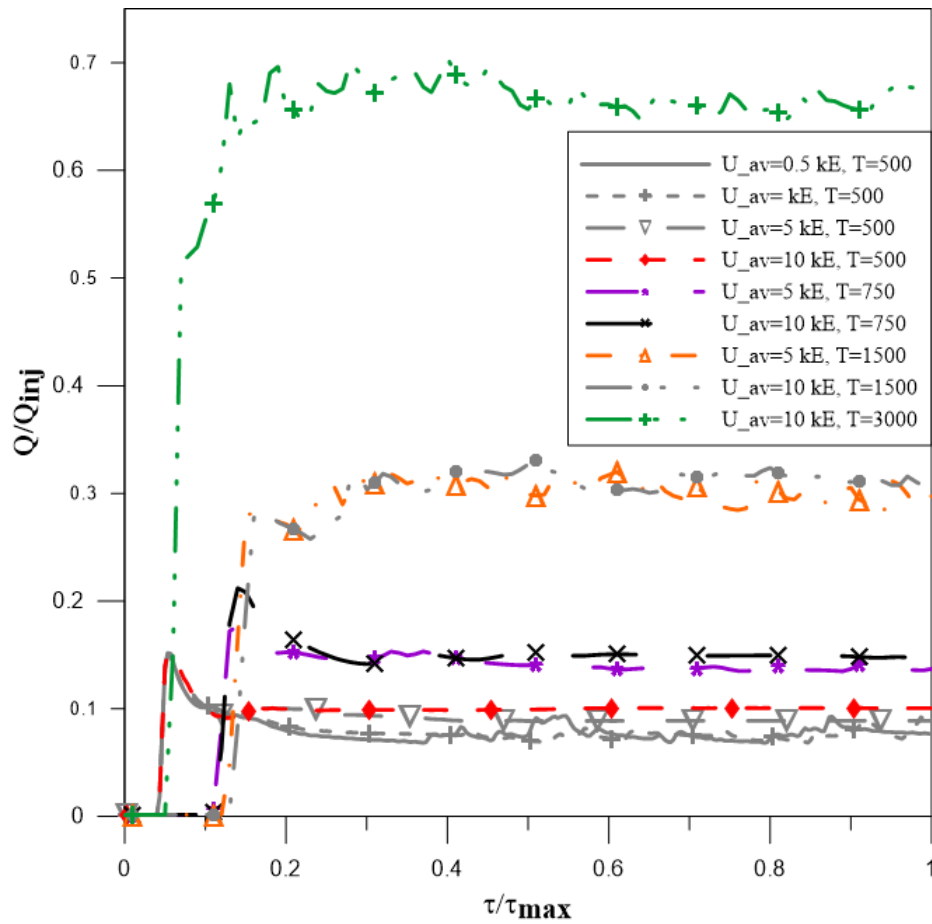


FIGURE 5.6: Spatially averaged normalised space charge versus normalised time as a function of T and U_{av}/kE .

6

Conclusions and future work

6.1 Introduction

This study has shown that the electrostatic atomiser has the potential to be used with biodiesel fuel. The important results from this investigation are summarised in this chapter. The main findings are presented into two parts: firstly, the effect of charge on FAME's droplet vaporisation; and secondly, the charge distribution between the electrodes. Recommendations for future studies on this topic are suggested at the end of this chapter.

6.2 Main Findings

6.2.1 The effect of charge on FAMEs' droplet vaporisation

A published mathematical model which already had been used to predict evaporation time of charged droplets for simpler fuels is extended to apply to other individual FAMEs. All of the model predictions are analysed concerning the experimentally relevant key parameters. The following are the key observations:

- With increasing initial charge density, the effect of charge increases for all the FAMEs regardless of the variation in chemical structures.
- Higher ambient temperatures decrease the effect of charge. The vaporisation time difference is found to be higher for C18:0 throughout the range, in both cases, i.e. the charge-only case and the charge+combustion case. Besides, for sibling combustion, the evaporation constant is found to play an important role in determining the sensitivity of charge for various FAMEs.
- A mixed effect is observed for droplet Reynolds numbers. For the charge-only case, increasing the droplet Reynolds number results in depletion of the charge sensitivity for all the FAMEs. However, with reference to sibling combustion, the charge sensitivity increases throughout the range.

6.2.2 The charge distribution between the electrodes

Existing direct numerical simulation data are examined to increase our fundamental understanding of charge transportation and their distribution at inter-electrode gap for a simple charge-injection system. The findings in this analysis are as follows:

- Higher instability in the flow helps to strip more charges from the emitter electrode.
- A high-flow-rate atomiser can reduce the leakage current.
- For a particular value of the electrical Rayleigh number, increasing the flow velocity can reduce instabilities, and when the velocity becomes sufficiently high, the flow in turn becomes stable.
- At a value of $T \geq 1500$, an increase in bulk-flow velocity resulted in stretching the roll

structures, which helps to lower the charge stratification in the middle of the domain.

6.3 Future work

To extend our knowledge of this topic the following suggestions are made regarding future avenues of research:

- The effect of charge on various FAMES' vaporisation can be experimentally investigated. An electrostatic atomiser can be used to inject FAMES, and spray current can be measured so that the charge sensitivity among them can be observed. During this measurement the bulk-flow velocity and electrical Rayleigh number can be varied according to the outcomes of this investigation. What is important is to observe the effect of the charge distribution at inter-electrode gap by watching the spray-specific charge.
- A computational study can be conducted to simulate the whole charge-injection and transportation process for an electrostatic atomiser.



Appendix

Appendix A

Droplet vaporisation modelling code for biodiesel fuel

```
1 % Droplet vaporisation modelling
2 close all;
3 clear all;
4 clc
5 %A. KOURMATZIS & Tushar Ahmed
6 %Initial values and step
7 t(1)=0;           %initial time (usually 0)
8 Td(1)=298;        %initial droplet temperature
9 D(1)=.001;        %initial droplet diameter in m
10 f2=1;            %coefficient used in Ranz-Marshall Correlation
11 comb=2;          %combustion modelled comb=1; 2=non-reacting
12 stagnant=1;      %stagnant=1 means the droplet is stationary;
13                 %stagnant=2 for mivong drops PXP
14 ui=10;           %initial gas velocity m/s
15 vi(1)=0;         %initial droplet velocity (0 if droplet stagnant)
16 s(1)=0;          %initail droplet position
17 g=9.81;          %acceleration due to gravity
18 fuel=14;         %7=C12:0,8=C14:0, 9=C16:0, 10=C18:0,
```

```

19          %11=C16:1, 12=C18:1; 13=C18:2; 14=C18:3
20  nsteph=10000;      %number of timesteps
21  tmax=90;          %maximum time in seconds
22  R=8314.5;         %universal gas constant
23  %Global Air Properties
24  Yg=0;             %mass fraction of vapour far from droplet surface
25  Wc=28.97;         %molar mass
26  Patm=1e5;         %standard pressure
27  dens_g=1.2;       %ambient density
28  Tg=373;          %ambient temperature
29  Pg=1e5;           %ambient pressure
30  %EHD conditions
31  Qpercini=0.58;    %initial droplet charge w.r.t. Rayleigh limit
32  Qres=0.8;         %residual droplet charge after fragmentation
33  EHD=1;            %EHD=1 charge ON, EHD=2 charge OFF
34  n=5;              %number of siblings after Coulombic Explosion
35  %Plot/calc properties
36  plotfunc=5;
37  choice=3;
38  sibcount=0;
39  for EHD.CHARGE=EHD; %Set to 2, for NO Charge calculation
40  for Q=fuel;
41      fuel_type=Q;
42      p=0; %FOR SUBPLOTS (graph counter)
43      j=0;
44  end
45  end
46  %Properties according to what fuel is simulated
47  if fuel_type==7 %C12:0; start add by PXP,
48      n_acid=12; %number of carbon atoms in carbon chain
49      DB=0; %number of double bonds
50      Wv=214.338; %Molecular weight; TableA2 pp567 Shanzin14
51      a_T=((7.536)/(log(n_acid)+3.584))-0.446;
52      dens_d=851.471+((250.718*DB+280.899)/(1214+n_acid))-a_T*4.85;
53      sigma=0.025; % viscosity
54      Tb=348.7+0.8478*Wv; %boiling point,
55      Tcr=534.3+.784*Wv; %critical point,
56      apl=1.816; %Shazin Fuel 115, Pages 559 572, 2014
57      bpl=-1.463e-3; %Shazin Fuel 115, Pages 559 572, 2014
58      cpl=7.51e-6; %saturated FAMES from C12 to C24 use the same eq
59      Cl=(apl+bpl*(Tg+Tb)/2+cpl*((Tg+Tb)/2)^2)*10^3;
60      nu_af=12.5; %Stoich A/F ratio;
61      dhc=37.89523316e6; %Heat of combustion J/kg;
62  elseif fuel_type==8 %C14:0; start add by PXP,
63      n_acid=14; %number of carbon atoms in carbon chain
64      DB=0; %number of double bonds
65      Wv=242.39; %Molecular weight; TableA2 pp567 Shanzin14
66      a_T=((7.536)/(log(n_acid)+3.584))-0.446;
67      dens_d=851.471+((250.718*DB+280.899)/(1214+n_acid))-a_T*4.85;
68      sigma=0.025;
69      Tb=348.7+0.8478*Wv; %boiling point,
70      Tcr=534.3+.784*Wv; %critical point,
71      apl=1.816;
72      bpl=-1.463e-3;
73      cpl=7.51e-6;
74      Cl=(apl+bpl*(Tg+Tb)/2+cpl*((Tg+Tb)/2)^2)*10^3;
75      nu_af=12.77;
76      dhc=38.9330218e6;
77  elseif fuel_type==9 %C16:0; start add by PXP,
78      n_acid=16;
79      DB=0;

```

```

80      Wv=270.442;
81      a_T=((7.536)/(log(n_acid)+3.584))- .446;
82      dens_d=851.471+((250.718*DB+280.899)/(1214+n_acid))-a_T*4.85;
83      sigma=0.02847;
84      Tb=348.7+.8478*Wv;
85      Tcr=534.3+.784*Wv;
86      apl=1.816;
87      bpl=-1.463e-3;
88      cpl=7.51e-6;
89      Cl=(apl+bpl*(Tg+Tb)/2+cpl*((Tg+Tb)/2)^2)*10^3;
90      nu_af=12.97037037;
91      dhc=39.4774e6;
92  elseif fuel_type==10 %C18:0;    start add by PXP,
93      n_acid=18;
94      DB=0;
95      Wv=298.494;
96      a_T=((7.536)/(log(n_acid)+3.584))- .446;
97      dens_d=851.471+((250.718*DB+280.899)/(1214+n_acid))-a_T*4.85;
98      sigma=0.025;
99      Tb=349.7+0.8478*Wv;
100     Tcr=534.3+.784*Wv;
101     apl=1.816;
102     bpl=-1.463e-3;
103     cpl=7.51e-6;
104     Cl=(apl+bpl*(Tg+Tb)/2+cpl*((Tg+Tb)/2)^2)*10^3;
105     nu_af=13.13422819;
106     dhc=40.10149624e6;
107  elseif fuel_type==11 %C16:1;    start add by PXP,
108     n_acid=16;
109     DB=1;
110     Wv=268.426;
111     a_T=((7.536)/(log(n_acid)+3.584))- .446;
112     dens_d=851.471+((250.718*DB+280.899)/(1214+n_acid))-a_T*5.85;
113     sigma=0.025;
114     Tb=350.4+Wv*0.8463;
115     Tcr=538.5+0.777*Wv;
116     apl=1.915;
117     bpl=-2.163e-3;
118     cpl=8.29e-6;
119     Cl=(apl+bpl*(Tg+Tb)/2+cpl*((Tg+Tb)/2)^2)*10^3;
120     nu_af=12.81094527;
121     dhc=39.32151964e6;
122  elseif fuel_type==12 %methyl oleate
123     n_acid=18;
124     DB=1;
125     Wv=296.5;
126     Tb=350.4+.8463*(296.478);
127     Tcr=538.5+.777*Wv;
128     nu_af=12.991;
129     a_T=((7.536)/(log(n_acid)+3.584))- .446;
130     dens_d=851.471+((250.718*DB+280.899)/(1214+n_acid))-a_T*4.85;
131     sigma=0.025;
132     apl=1.915;
133     bpl=-2.163e-3;
134     cpl=8.29e-6;
135     Cl=(apl+bpl*(Tg+Tb)/2+cpl*((Tg+Tb)/2)^2)*10^3;
136     dhc=39.9364043e6;
137  elseif fuel_type==13 %C18:2;    start add by PXP,
138     n_acid=18;
139     DB=2;
140     Wv=294.462;

```

```

141     a_T=((7.536)/(log(n_acid)+3.584))- .446;
142     dens_d=851.471+((250.718*DB+280.899)/(1214+n_acid))-a_T*5.85;
143     sigma=0.025;
144     Tb=352.1+Wv*0.8463;
145     Tcr=542.6+0.772*Wv;
146     apl=2.018;
147     bpl=-2.878e-3;
148     cpl=9.09e-6;
149     Cl=(apl+bpl*(Tg+Tb)/2+cpl*((Tg+Tb)/2)^2)*10^3;
150     nu_af=12.84580499;
151     dhc=39.7263964e6;
152     elseif fuel_type==14 %C18:3; start add by PXP,
153         n_acid=18;
154         DB=3;
155         Wv=292.446;
156         a_T=((7.536)/(log(n_acid)+3.584))- .446;
157         dens_d=851.471+((250.718*DB+280.899)/(1214+n_acid))-a_T*5.85;
158         sigma=0.025;
159         Tb=353.82+0.8472*Wv;
160         Tcr=546.8+0.7711*Wv;
161         apl=2.115;
162         bpl=-3.580e-3;
163         cpl=9.92e-6;
164         Cl=(apl+bpl*(Tg+Tb)/2+cpl*((Tg+Tb)/2)^2)*10^3;
165         nu_af=12.69863014;
166         dhc=39.37032826e6;
167         elseif fuel_type==15
168             dens_d=838;
169             sigma=0.02996;
170     end
171     theta_2=Wc/Wv;
172     ratio=R/Wv;
173     for l=1:1 %diameter loop
174         Qrayi=(pi*(8.85e-12*sigma)^(1/2))*(2*D(l))^(3/2);
175         Qi=Qpercini*Qrayi;
176         dth = (tmax-t(1))/nsteph;
177         m(1)=((4/3)*pi*((D(1)/2)^3))*dens_d;
178         Di(1)=D(1);
179         D_sq(1)=Di(1)^2;
180 %%%%%%%%%%%%%%%%%%%%%%%%%%%%%%%%%%%%%%%%%%%%%%%%%%%%%%%%%%%%%%%%%%%%%%%%%%CALCULATE PROPERTIES AND IMPLEMENT RK4%%%%%%%%%%%%%%%%%%%%%%%%%%%%%%%%%%%%%%%%%%%%%%%%%%%%%%%%%%%%%%%%%%%%%%%%%
181     for j=1:nsteph
182         Twb=(Tb+Tg)/2;
183         Tr=Td(j)+1/3*(Tg-Td(j));
184         visc_g= 6.109e-6 + 4.604e-8*(Twb) - 1.051e-11*(Twb^2);
185         tau_dt=(dens_d*(Di(j)^2))/(18*visc_g);
186         if stagnant==1
187             Re=(dens_g*Di(j)*ui)/visc_g;
188         elseif stagnant==2
189             Re=((dens_g*Di(j))*abs(ui-vi(j)))/visc_g;
190         end
191         Res(j)=Re;
192         absvel(j)=abs(ui-vi(j));
193         if Twb<600
194             Prg=.815 - 4.958e-4*(Twb) + 4.514e-7*(Twb^2);
195         elseif Twb>600
196             Prg=.647 + 5.5e-5*(Twb);
197         end
198         Nu= 2 + 0.552*(Re^(1/2))*(Prg^(1/3));
199         lambda_air= 3.227e-3 + 8.3894e-5*(Twb) - 1.9858e-8*(Twb^2);
200         theta_1=((Prg*lambda_air)/(visc_g))/Cl; %air/fuel
201         cp_g=((Prg*lambda_air)/(visc_g));

```

```

202         if fuel_type==7 %methyl xxx; C12:0
203             phi_L=((Tcr-Twb)/(Tcr-Tb))^(0.38);
204             Lv_t=((1.506e7+(1.814e5)*(Wv))*phi_L)/Wv;
205             lambda_fg=lambda_air;
206             Tflame=2450; %Jha et al. Fuel 2008
207             cp_fg=0.027532*(Twb/300)^5-2.50961*(Twb/300)^4+32.489208*
208                 (Twb/300)^3-348.51699*(Twb/300)^2+...
209                 1937.2422*(Twb/300) -196.0638;
210         elseif fuel_type==8 %methyl xxx; C14:0
211             phi_L=((Tcr-Twb)/(Tcr-Tb))^(0.38);
212             Lv_t=((1.506e7+(1.814e5)*(Wv))*phi_L)/Wv;
213             lambda_fg=lambda_air;
214             Tflame=2500; %Jha et al. Fuel 2008
215             cp_fg=0.028031*(Twb/300)^5-1.537655*(Twb/300)^4+33.11172*
216                 (Twb/300)^3-355.3911*(Twb/300)^2+...
217                 1975.95*(Twb/300) -217.793;
218         elseif fuel_type==9 %methyl xxx; C16:0
219             phi_L=((Tcr-Twb)/(Tcr-Tb))^(0.38);
220             Lv_t=((1.506e7+(1.814e5)*(Wv))*phi_L)/Wv;
221             lambda_fg=lambda_air;
222             Tflame=2525; %K%Jha et al. Fuel 2008
223             cp_fg=0.02847*(Twb/300)^5 - 1.562807*Twb/300)^4 + 33.666284*
224                 (Twb/300)^3 -353.10969*(Twb/300)^2 +...
225                 2008.022573*(Twb/300) -236.281242;
226     elseif fuel_type==10 %methyl xxx; C18:0
227         phi_L=((Tcr-Twb)/(Tcr-Tb))^(0.38);
228         Lv_t=((1.506e7+(1.814e5)*(Wv))*phi_L)/Wv;
229         lambda_fg=lambda_air; %dilute assumption as in Sahzin et al.
230         Tflame=2540; %K%Jha et al. Fuel 2008
231         cp_fg=0.029073*(Twb/300)^5-1.592711*(Twb/300)^4+34.24248*(Twb/300)^3
232             -366.8571*(Twb/300)^2+...
233             2035.689*(Twb/300) -252.356;
234     elseif fuel_type==11 %methyl xxx; C16:1
235         phi_L=((Tcr-Twb)/(Tcr-Tb))^(0.38);
236         Lv_t=((1.389e7+(1.822e5)*(Wv))*phi_L)/Wv; %latent heat of evaporation,
237         lambda_fg=lambda_air; %dilute assumption as in Sahzin et al.
238         Tflame=2525; %K%assume to be similar to C16:0, Jha et al. Fuel 2008
239         cp_fg=0.028355*(Twb/300)^5-1.548214*(Twb/300)^4+33.141987*(Twb/300)^3
240             -353.10969*(Twb/300)^2+...
241             1946.7159*(Twb/300) -194.6743;
242     elseif fuel_type==12 %methyl oleate; C18:1
243         phi_L=((Tcr-Twb)/(Tcr-Tb))^(0.38);
244         Lv_t=((1.389e7+(1.882e5)*(Wv))*phi_L)/Wv; %latent heat of evaporation
245         lambda_fg=lambda_air; %dilute assumption as in Sahzin et al.
246         Tflame=2340; %Jha et al. Fuel 2008
247         cp_fg=0.028632*(Twb/300)^5-1.565423*(Twb/300)^4+33.556761*(Twb/300)^3
248             -358.027218*(Twb/300)^2+...
249             1976.32596*(Twb/300)-210.68717;
250     elseif fuel_type==13 %methyl xxx; C18:2
251         phi_L=((Tcr-Twb)/(Tcr-Tb))^(0.38);
252         lambda_fg=lambda_air; %dilute assumption as in Sahzin et al.
253         Tflame=2540; %K%assume to be similar to C18:0, Jha et al. Fuel 2008
254         cp_fg=0.028537*(Twb/300)^5-1.552823*(Twb/300)^4+33.097465*(Twb/300)^3
255             -350.761281*(Twb/300)^2+...
256             1921.716581*(Twb/300) -176.117655;
257     elseif fuel_type==14 %methyl xxx; C18:3
258         phi_L=((Tcr-Twb)/(Tcr-Tb))^(0.38);
259         Lv_t=((1.154e7+(1.834e5)*(Wv))*phi_L)/Wv; %latent heat of evaporation,
260         lambda_fg=lambda_air; %dilute assumption as in Sahzin et al.
261         Tflame=2540; %K%assume to be similar to C18:0, Jha et al. Fuel 2008
262         cp_fg=0.02823*(Twb/300)^5-1.531367*(Twb/300)^4+32.505573*(Twb/300)^3

```

```

263     -342.625176*(Twb/300)^2+...
264     1864.607187*(Twb/300) -140.492938;
265     end
266     xseqt(j)=(Patm/Pg)*exp((Lv_t/ratio)*(1/Tb-1/Td(j)));
267     Yseq_t=xseqt(j)/(xseqt(j)+(1-xseqt(j))*theta_2);
268     Yr=Yseq_t+(1/3)*(Yg-Yseq_t);
269     diff_g=lambda_air/(dens_g*cp_g);
270     %Scg=Prg since Le=1
271     Sc_t=Prg;
272     Sh_t=2 + 0.552*(Re^(1/2))*(Sc_t^(1/3));
273     Bmeq_t(j)=(Yseq_t-Yg)/(1-Yseq_t);
274     Hm_t=log(1+Bmeq_t(j));
275     % 4th order Explicit Runge-Kutta Scheme
276     K1=dth*(f2*(Nu/(3*Prg))*(theta_1/tau_dt)*(Tg-Td(j))
277 + (Lv_t/C1)*((-Sh_t/(3*Sc_t*tau_dt))*Hm_t));
278     K2=dth*(f2*(Nu/(3*Prg))*(theta_1/tau_dt)*(Tg-(Td(j)+(K1/2)))
279 + (Lv_t/C1)*((-Sh_t/(3*Sc_t*tau_dt))*Hm_t));
280     K3=dth*(f2*(Nu/(3*Prg))*(theta_1/tau_dt)*(Tg-(Td(j)+(K2/2)))
281 + (Lv_t/C1)*((-Sh_t/(3*Sc_t*tau_dt))*Hm_t));
282     K4=dth*(f2*(Nu/(3*Prg))*(theta_1/tau_dt)*(Tg-(Td(j)+K3))
283 + (Lv_t/C1)*((-Sh_t/(3*Sc_t*tau_dt))*Hm_t));
284     Td(j+1)=Td(j)+(1/6)*(K1+(2*K2)+(2*K3)+K4);
285     K1m=dth*((( -Sh_t/(3*Sc_t))*(m(j)/tau_dt))*Hm_t);
286     K2m=dth*((( -Sh_t/(3*Sc_t))*(m(j)+(K1m/2))/tau_dt))*Hm_t);
287     K3m=dth*((( -Sh_t/(3*Sc_t))*(m(j)+(K2m/2))/tau_dt))*Hm_t);
288     K4m=dth*((( -Sh_t/(3*Sc_t))*(m(j)+K3m)/tau_dt))*Hm_t);
289     m(j+1)=m(j)+(1/6)*(K1m+(2*K2m)+(2*K3m)+K4m);
290     Di(j+1)=((24*m(j+1))/(4*dens_d*pi))^(1/3);
291     D_sq(j+1)=Di(j+1)^2;
292     beta(j+1)=-((3*Prg*tau_dt)/2)*(((m(j+1)-m(j))/dth)/(m(j+1)));
293     G(j+1)=beta(j+1)/(exp(beta(j+1))-1);
294     f2=G(j+1);
295     end
296     if EHD.CHARGE==1
297         Q=(Qi)/(4/3*pi*(Di(j)/2)^3);
298         Qray=(pi*(8.85e-12*sigma)^(1/2))*(2*Di(j))^(3/2);
299         Qrayv=Qray/(4/3*pi*(Di(j)/2)^3);
300         charge(j)=Q/Qrayv;
301         if .8*Qrayv<Q;
302             sibcount=sibcount+1;
303             m_core(sibcount)=.975*m(j);
304             Di_core(sibcount)=((24*m_core(sibcount))/(4*dens_d*pi))^(1/3);
305             m_sibi(sibcount)=(1-.975)/n*m(j);
306             Di_sibi(sibcount)=((24*m_sibi(sibcount))/(4*dens_d*pi))^(1/3);
307             if comb==1
308                 Bq=((dhc/nu_af)+cp_fg*(Tg-Tb))/Lv_t;
309                 lambda_g=(0.4*lambda_fg)+(0.6*lambda_air);
310                 K=((8*lambda_g)/(cp_fg*dens_d))*log(1+Bq);
311                 t_evap=(Di_sibi(sibcount).^2)/K;
312                 n_timesteps(sibcount)=t_evap/dth;
313                 dtsmall=(t_evap/(nsteph/100));
314                 mc(1)=.975*m(j);
315                 Dic(1)=Di_core(sibcount);
316                 Tds(1)=Td(j);
317                 vis(1)=vi(j);
318                 ts(1)=t(j+1);
319             for count=1:(nsteph/100)
320                 ts(count+1)=ts(1)+count*dtsmall;
321                 Tp=(Twb);
322                 visc_g= 6.109e-6 + 4.604e-8*(Tp) - 1.051e-11*(Tp^2);
323                 tau_dt=(dens_d*(Dic(count)^2))/(18*visc_g);

```

```

324     if stagnant==1
325         Re=(dens_g*Dic(count)*ui)/visc_g;
326     elseif stagnant==2
327         Re=((dens_g*Dic(count))*abs(ui-vis(count)))/visc_g;
328     end
329     Prg=.647 - (5.5e-5)*(Tp); %greater than 600K only!
330     Nu= 2 + 0.552*(Re^(1/2))*(Prg^(1/3));
331     lambda_air= 3.227e-3 + 8.3894e-5*(Tp) - 1.9858e-8*(Tp^2);
332     theta_1=((Prg*lambda_air)/(visc_g))/Cl; %air/fuel
333     cp_g=((Prg*lambda_air)/(visc_g));
334     xseqts(count)=(Patm/Pg)*exp((Lv_t/ratio)*(1/Tb-1/Tds(count)));
335     Yseq_ts=xseqts(count)/(xseqts(count)+(1-xseqts(count))*theta_2);
336     Yrs=Yseq_ts+(1/3)*(Yg-Yseq_ts);
337     diff_g=lambda_air/(dens_g*cp_g);
338     %Scg=Prg since Le=1
339     Sc_t=Prg;
340     Sh_t=2 + 0.552*(Re^(1/2))*(Sc_t^(1/3));
341     Bmeq_ts(count)=(Yseq_ts-Yg)/(1-Yseq_ts);
342     Hm_ts=log(1+Bmeq_ts(count));
343     % 4th order Explicit Runge-Kutta Scheme
344     K1s=dtsmall*(f2*(Nu/(3*Prg))*(theta_1/tau_dt)*(((Tflame+Tg)/2)-Tds(count))
345     + (Lv_t/Cl)*((-Sh_t/(3*Sc_t*tau_dt))*Hm_ts));
346     K2s=dtsmall*(f2*(Nu/(3*Prg))*(theta_1/tau_dt)*(((Tflame+Tg)/2)-(Tds(count)
347     +(K1s/2))) + (Lv_t/Cl)*((-Sh_t/(3*Sc_t*tau_dt))*Hm_ts));
348     K3s=dtsmall*(f2*(Nu/(3*Prg))*(theta_1/tau_dt)*(((Tflame+Tg)/2)-(Tds(count)
349     +(K2s/2))) + (Lv_t/Cl)*((-Sh_t/(3*Sc_t*tau_dt))*Hm_ts));
350     K4s=dtsmall*(f2*(Nu/(3*Prg))*(theta_1/tau_dt)*(((Tflame+Tg)/2)-(Tds(count)
351     +K3s)) + (Lv_t/Cl)*((-Sh_t/(3*Sc_t*tau_dt))*Hm_ts));
352     Tds(count+1)=Tds(count)+(1/6)*(K1s+(2*K2s)+(2*K3s)+K4s);
353     K1ms=dtsmall*((( -Sh_t/(3*Sc_t))*(mc(count)/tau_dt))*Hm_ts);
354     K2ms=dtsmall*((( -Sh_t/(3*Sc_t))*((mc(count)+(K1ms/2))/tau_dt))*Hm_ts);
355     K3ms=dtsmall*((( -Sh_t/(3*Sc_t))*((mc(count)+(K2ms/2))/tau_dt))*Hm_ts);
356     K4ms=dtsmall*((( -Sh_t/(3*Sc_t))*((mc(count)+(K3ms)/tau_dt))*Hm_ts);
357     mc(count+1)=mc(count)+(1/6)*(K1ms+(2*K2ms)+(2*K3ms)+K4ms);
358     Dic(count+1)=((24*mc(count+1))/(4*dens_d*pi))^(1/3);
359     D_sqc(count+1)=Dic(count+1).^2;
360     mco=mc(count+1);
361     Dco=Dic(count+1);
362     Dcos=D_sqc(count+1);
363     fls=1+(1/6)*(Re)^(2/3);
364     vis(count+1)=vis(count)+dth*((fls/tau_dt)*(ui-vis(count))+g);
365     a_s=((vis(count+1)-vis(count))/dth);
366     ss(count+1)=(((vis(count+1))^2-(vis(count))^2)/(2*a))+ss(count);
367     %distance traveled
368     D_sqc(1)=Dic(1).^2;
369     Dstore(sibcount,count)=D_sqc(count+1);
370     Dstore2(sibcount,count)=Dic(count+1);
371     tstore(sibcount,count)=ts(count+1);
372     end
373     else
374         mco=m_core(sibcount);
375         Dco=Di_core(sibcount);
376         Dcos=Di_core(sibcount)^2;
377         t_evap=0;
378     end
379     elseif Q<.8*Qrayv;
380         mco=m(j+1);
381         Dco=Di(j+1);
382         Dcos=D_sq(j+1);
383         t_evap=0;
384     end

```

```

385             m(j+1)=mco;
386             Di(j+1)=Dco;
387             D_sq(j+1)=Dcos;
388         elseif EHD_CHARGE==2
389             m(j+1)=m(j+1);
390             Di(j+1)=Di(j+1);
391             D_sq(j+1)=D_sq(j+1);
392             t_evap=0;
393         end
394     t(j+1)=t(j)+dth+t_evap;
395     if m(j+1)<=m(1)*.0001
396         break;
397     end
398 end

```

Appendix B

DNS data post-processing code for Fig.5.5

```

1  clear all
2  close all
3  clc
4  % Tushar Ahmed & A. KOURMATZIS
5
6  % The following is a data processing code.
7
8  folder_name=uigetdir('C:\Users\44733496\Desktop\ForTushar');
9  filenameExtension= '.dat';
10 % target=0.0005;
11 % target=0.000438;
12 % target=0.000403;
13 TempMatrix=zeros(0,8); %pre-allocation
14 for i=6000:100:10000
15     filename=[folder_name, '\data', int2str(i), filenameExtension];
16     textData=dlmread(filename, ',',1,0);
17     textData(:,8)=textData(i);
18     OneMatrix=[TempMatrix;textData];
19     TempMatrix=OneMatrix;
20     for target=0.0005;
21         v=find(TempMatrix(:,2)==target);
22         t=OneMatrix(v,:);
23         n=80;
24         tmp=reshape(t,[n prod(size(t))/n]);
25         tmp=mean(tmp);
26         matrix_avg=reshape(tmp,[size(t,1)/n size(t,2)]);
27         a=mean(matrix_avg);
28     end
29     for target=0.000451;
30         v=find(TempMatrix(:,2)==target);
31         t=OneMatrix(v,:);
32         n=80;
33         tmp=reshape(t,[n prod(size(t))/n]);
34         tmp=mean(tmp);
35         matrix_avg=reshape(tmp,[size(t,1)/n size(t,2)]);
36         b=mean(matrix_avg);
37     end
38     for target=0.000403;

```

```

39     v=find (TempMatrix(:,2)== target );
40     t=OneMatrix (v, : );
41     n=80;
42     tmp=reshape (t, [n prod (size (t))/n]);
43     tmp=mean (tmp);
44     matrix_avg=reshape (tmp, [size (t,1)/n size (t,2)]);
45     c=mean (matrix_avg);
46     end
47     for target=0.000393;
48     v=find (TempMatrix(:,2)== target );
49     t=OneMatrix (v, : );
50     n=80;
51     tmp=reshape (t, [n prod (size (t))/n]);
52     tmp=mean (tmp);
53     matrix_avg=reshape (tmp, [size (t,1)/n size (t,2)]);
54     d=mean (matrix_avg);
55     end
56     for target=0.000353;
57     v=find (TempMatrix(:,2)== target );
58     t=OneMatrix (v, : );
59     n=80;
60     tmp=reshape (t, [n prod (size (t))/n]);
61     tmp=mean (tmp);
62     matrix_avg=reshape (tmp, [size (t,1)/n size (t,2)]);
63     e=mean (matrix_avg);
64     end
65     for target=0.000316;
66     v=find (TempMatrix(:,2)== target );
67     t=OneMatrix (v, : );
68     n=80;
69     tmp=reshape (t, [n prod (size (t))/n]);
70     tmp=mean (tmp);
71     matrix_avg=reshape (tmp, [size (t,1)/n size (t,2)]);
72     f=mean (matrix_avg);
73     end
74     for target=0.000292;
75     v=find (TempMatrix(:,2)== target );
76     t=OneMatrix (v, : );
77     n=80;
78     tmp=reshape (t, [n prod (size (t))/n]);
79     tmp=mean (tmp);
80     matrix_avg=reshape (tmp, [size (t,1)/n size (t,2)]);
81     g=mean (matrix_avg);
82     end
83     for target=0.000235;
84     v=find (TempMatrix(:,2)== target );
85     t=OneMatrix (v, : );
86     n=80;
87     tmp=reshape (t, [n prod (size (t))/n]);
88     tmp=mean (tmp);
89     matrix_avg=reshape (tmp, [size (t,1)/n size (t,2)]);
90     h=mean (matrix_avg);
91     end
92     for target=0.000208;
93     v=find (TempMatrix(:,2)== target );
94     t=OneMatrix (v, : );
95     n=80;
96     tmp=reshape (t, [n prod (size (t))/n]);
97     tmp=mean (tmp);
98     matrix_avg=reshape (tmp, [size (t,1)/n size (t,2)]);
99     j=mean (matrix_avg);

```

```

100         end
101         for target=0.000184;
102 v=find (TempMatrix(:,2)==target);
103 t=OneMatrix(v,:);
104 n=80;
105 tmp=reshape(t,[n prod(size(t))/n]);
106 tmp=mean(tmp);
107 matrix_avg=reshape(tmp,[size(t,1)/n size(t,2)]);
108 k=mean(matrix_avg);
109         end
110         for target=0.000147;
111 v=find (TempMatrix(:,2)==target);
112 t=OneMatrix(v,:);
113 n=80;
114 tmp=reshape(t,[n prod(size(t))/n]);
115 tmp=mean(tmp);
116 matrix_avg=reshape(tmp,[size(t,1)/n size(t,2)]);
117 l=mean(matrix_avg);
118         end
119         for target=0.000107;
120 v=find (TempMatrix(:,2)==target);
121 t=OneMatrix(v,:);
122 n=80;
123 tmp=reshape(t,[n prod(size(t))/n]);
124 tmp=mean(tmp);
125 matrix_avg=reshape(tmp,[size(t,1)/n size(t,2)]);
126 m=mean(matrix_avg);
127         end
128         for target=0.000097;
129 v=find (TempMatrix(:,2)==target);
130 t=OneMatrix(v,:);
131 n=80;
132 tmp=reshape(t,[n prod(size(t))/n]);
133 tmp=mean(tmp);
134 matrix_avg=reshape(tmp,[size(t,1)/n size(t,2)]);
135 o=mean(matrix_avg);
136         end
137         for target=0.00005;
138 v=find (TempMatrix(:,2)==target);
139 t=OneMatrix(v,:);
140 n=80;
141 tmp=reshape(t,[n prod(size(t))/n]);
142 tmp=mean(tmp);
143 matrix_avg=reshape(tmp,[size(t,1)/n size(t,2)]);
144 p=mean(matrix_avg);
145         end
146         for target=0.000000;
147 v=find (TempMatrix(:,2)==target);
148 t=OneMatrix(v,:);
149 n=80;
150 tmp=reshape(t,[n prod(size(t))/n]);
151 tmp=mean(tmp);
152 matrix_avg=reshape(tmp,[size(t,1)/n size(t,2)]);
153 q=mean(matrix_avg);
154         end
155 end
156 r=[a(5) b(5) c(5) d(5) e(5) f(5) g(5) h(5) j(5) k(5) l(5) m(5) o(5) p(5) q(5)];
157 s=r/.0036;
158 n=80;
159 tmp=reshape(t,[n prod(size(t))/n]);
160 tmp=mean(tmp);

```

```

161 matrix_avg=reshape(tmp,[size(t,1)/n size(t,2)]);
162 z=matrix_avg;
163 q =z(:,5)/.0006;
164 t =0.002:0.002:.6;          %U_av=0.5kE_ReE=1;  U_av=5kE_Re_E=1;
165                               %U_av=10kE, Re=10.4;  U_av=kE_Re_E=1
166 %t=0.0005:0.0005:0.15;      %U_av=kE_Re_E=60
167 %t=.0004:.0004:.12;        %U_av=kE_Re_E=120
168 %t=0.001:.001:.1;
169 %t=.002:.002:.2;
170 %t=.004:.004:.4;

```

DNS data post-processing code for Fig.5.6

```

1  clear all
2  close all
3  clc
4  % Tushar Ahmed & A. KOURMATZIS
5  % The following is a data processing code.
6  folder_name=uigetdir
7  ( 'C:\Users\44733496\Desktop\ForTushar\morehedcases\C=10,Re_E=1' );
8  %copy the data folder directory
9  filenameExtension= '.dat';
10 %target=0.000403;
11 TempMatrix=zeros(0,8); %pre-allocation
12 target=.000235;
13 select=3; %1= velocity, 2=pressure, 3=charge,
14 %4=electric field, 5= velocity in x direction
15 for i=6100:100:10000
16     filename=[folder_name, '\data', int2str(i), filenameExtension];
17     textData=dlmread(filename, ',',1,0);
18     textData(:,8)=textData(i);
19     OneMatrix=[TempMatrix;textData];
20     TempMatrix=OneMatrix;
21     % for target=.000021
22     v=find(TempMatrix(:,2)==target);
23     t=OneMatrix(v,:);
24     % end
25     % for target=.000403
26     % k=find(t(:,2)==target);
27     % g=t(k,:);
28     % end
29
30 end
31 n=80;
32 tmp=reshape(t,[n prod(size(t))/n]);
33 tmp=mean(tmp);
34 matrix_avg=reshape(tmp,[size(t,1)/n size(t,2)]);
35 z=matrix_avg;
36 q =z(:,5)/.0009;
37 % %q=t(:,5)/.0006;
38 % m=.00012:.00012:.012;
39 % plot(m,q);
40 % %t=0.002:.002:.6;          %U_av=0.5kE_ReE=1;  U_av=5kE_Re_E=1;
41 %                               %U_av=10kE, Re=10.4;  U_av=kE_Re_E=1
42 % % t=0.0005:0.0005:0.15;      %U_av=kE_Re_E=60
43 %t=.0004:.0004:.12;        %U_av=kE_Re_E=120
44 % %t=0.001:.001:.1;
45 % %t=.002:.002:.2;
46 % t=.00004:.00004:.00244;
47 m=.005:.005:.2;
48 plot(m,q);

```

```
49  if select==2;
50  plot(m,q);
51  xlabel('Time');
52  ylabel('Pressure');
53  title('Pressure Vs Time');
54  end
55  if select==3;
56      plot(t,q);
57
58  xlabel('Time');
59  ylabel('Charge');
60  title('Charge Vs Time');
61  end
62  if select==1
63      plot(t,z(:,3));
64      xlabel('Time');
65      ylabel('Velocity');
66      title('Velocity Vs Time');
67  end
68  if select==4
69      plot(t,z(:,7));
70      xlabel('Time');
71      ylabel('Electric field');
72      title('Electric field Vs Time');
73  end
74  if select==5
75      plot(t,z(:,2));
76      xlabel('Time');
77      ylabel('Velocity in x direction');
78      title('Velocity in x direction Vs Time');
79  end
```

References

- [1] L. Turrio-Baldassarri, C. L. Battistelli, L. Conti, R. Crebelli, B. De Berardis, A. L. Iamiceli, M. Gambino, and S. Iannaccone. *Emission comparison of urban bus engine fueled with diesel oil and biodieselblend*. Science of the Total Environment **327**(1), 147 (2004).
- [2] J. Bünger, J. Krahel, K. Baum, O. Schröder, M. Müller, G. Westphal, P. Ruhnau, T. Schulz, and E. Hallier. *Cytotoxic and mutagenic effects, particle size and concentration analysis of diesel engine emissions using biodiesel and petrol diesel as fuel*. Archives of toxicology **74**(8), 490 (2000).
- [3] M. Balat. *Global trends on the processing of bio-fuels*. International Journal of Green Energy **5**(3), 212 (2008).
- [4] M. Balat and H. Balat. *Progress in biodiesel processing*. Applied energy **87**(6), 1815 (2010).
- [5] G. Knothe, J. Krahel, and J. Van Gerpen. *The biodiesel handbook* (Elsevier, 2015).
- [6] M. S. Graboski and R. L. McCormick. *Combustion of fat and vegetable oil derived fuels in diesel engines*. Progress in energy and combustion science **24**(2), 125 (1998).
- [7] J. Hill, E. Nelson, D. Tilman, S. Polasky, and D. Tiffany. *Environmental, economic, and energetic costs and benefits of biodiesel and ethanol biofuels*. Proceedings of the National Academy of sciences **103**(30), 11206 (2006).

-
- [8] A. Shekarriz and J. G. Birmingham. *Electrostatic atomizer and method of producing atomized fluid sprays* (2004). US Patent 6,802,456.
 - [9] J. Shrimpton. *Charge injection systems: physical principles, experimental and theoretical work* (Springer Science & Business Media, 2009).
 - [10] G. Al-Ahmad, J. S. Shrimpton, E. Ergene, and F. Mashayek. *Electrical performance of a charge-injection atomizer using viscous organic oils*. *Atomization and Sprays* **19**(6) (2009).
 - [11] A. Kourmatzis. *Pulsed charge injection atomization and turbulent electrohydrodynamics*. Ph.D. thesis, University of Southampton (2011).
 - [12] M. Jido. *Study of electrostatic charged droplets : Part 1*. *J. Jpn. Soc. Chem. Eng.* **40**, 24 (1986).
 - [13] K. S. Robinson, R. J. Turnbull, and K. Kim. *Electrostatic spraying of liquid insulators*. *IEEE Transactions on Industry Applications* (2), 308 (1980).
 - [14] A. Rigit and J. S. Shrimpton. *Electrical performance of charge injection electrostatic atomizers*. *Atomization and Sprays* **16**(4) (2006).
 - [15] J. S. Shrimpton and Y. Laonual. *Dynamics of electrically charged transient evaporating sprays*. *International journal for numerical methods in engineering* **67**(8), 1063 (2006).
 - [16] A. Rigit and J. S. Shrimpton. *Estimation of the diameter-charge distribution in polydisperse electrically charged sprays of electrically insulating liquids*. *Experiments in fluids* **46**(6), 1159 (2009).
 - [17] A. Rigit and J. S. Shrimpton. *Spray characteristics of charge injection electrostatic atomizers with small-orifice diameters*. *Atomization and Sprays* **16**(4) (2006).
 - [18] Z.-T. Wang, A. M. Mitrašinović, and J. Z. Wen. *Investigation on electrostatic breakup of bio-oil droplets*. *Energies* **5**(11), 4323 (2012).

-
- [19] J. Barata. *Modelling of biofuel droplets dispersion and evaporation*. Renewable energy **33**(4), 769 (2008).
- [20] W. Hallett and N. Legault. *Modelling biodiesel droplet evaporation using continuous thermodynamics*. Fuel **90**(3), 1221 (2011).
- [21] K. Saha, E. Abu-Ramadan, and X. Li. *Multicomponent evaporation model for pure and blended biodiesel droplets in high temperature convective environment*. Applied energy **93**, 71 (2012).
- [22] S. Dirbude, V. Eswaran, and A. Kushari. *Droplet vaporization modeling of rapeseed and sunflower methyl esters*. Fuel **92**(1), 171 (2012).
- [23] M. H. Azami and M. Savill. *Modelling of spray evaporation and penetration for alternative fuels*. Fuel **180**, 514 (2016).
- [24] S. Sazhin, M. Al Qubeissi, R. Kolodnytska, A. Elwardany, R. Nasiri, and M. Heikal. *Modelling of biodiesel fuel droplet heating and evaporation*. Fuel **115**, 559 (2014).
- [25] M. Al Qubeissi, S. Sazhin, C. Crua, J. Turner, and M. Heikal. *Modelling of biodiesel fuel droplet heating and evaporation: effects of fuel composition*. Fuel **154**, 308 (2015).
- [26] E. L. Ergene. *Investigation of the Electrostatic Atomization Method for Remote Injection and High Pressure*. Ph.D. thesis (2012).
- [27] K. Kim and R. J. Turnbull. *Generation of charged drops of insulating liquids by electrostatic spraying*. Journal of Applied Physics **47**(5), 1964 (1976).
- [28] A. Kelly. *The electrostatic atomization of hydrocarbons*. J. Inst. Energy **57**, 312 (1984).
- [29] A. Yule, J. Shrimpton, A. Watkins, W. Balachandran, and D. Hu. *Electrostatically atomized hydrocarbon sprays*. Fuel **74**(7), 1094 (1995).
- [30] M. Jido. *Study of electrostatic charged droplets : Part 1*. J. Jpn. Soc. Chem. Eng. **40**, 24 (1986).

-
- [31] J. Allen, P. Ravenhill, and J. Shrimpton. *Spray characteristics of a novel multi orifice electrostatic atomizer*. In *Proceedings of the 20th ILASS Europe meeting*, pp. 373–377 (2005).
- [32] G. Malkawi. *Point-to-plane and plane-to-plane electrostatic charge injection atomization for insulating liquids* (2010).
- [33] A. Kourmatzis, J. Allen, and J. S. Shrimpton. *Electrical and spray characteristics of a multiorifice charge-injection atomizer for electrically insulating liquids*. *Atomization and Sprays* **20**(4) (2010).
- [34] K. Aung, M. Hassan, and G. Faeth. *Flame stretch interactions of laminar premixed hydrogen/air flames at normal temperature and pressure*. *Combustion and flame* **109**(1-2), 1 (1997).
- [35] R. Borghi. *The links between turbulent combustion and spray combustion and their modelling*. In *8th International Symposium on Transport Phenomena in Combustion*, pp. 1–18 (1996).
- [36] M. Sommerfeld and H.-H. Qiu. *Experimental studies of spray evaporation in turbulent flow*. *International journal of heat and fluid flow* **19**(1), 10 (1998).
- [37] R. Miller, K. Harstad, and J. Bellan. *Evaluation of equilibrium and non-equilibrium evaporation models for many-droplet gas-liquid flow simulations*. *International Journal of Multiphase Flow* **24**(6), 1025 (1998).
- [38] A. Kourmatzis. *Sensitivities in the modeling of electrostatically charged droplet evaporation and combustion*. *Journal of Energy Engineering* **143**(3), 04016060 (2016).
- [39] W. Ranz, W. Marshall, *et al.* *Evaporation from drops*. *Chem. Eng. Prog* **48**(3), 141 (1952).
- [40] A. H. Lefebvre. *Fuel effects on gas turbine combustion-liner temperature, pattern factor, and pollutant emissions*. *Journal of Aircraft* **21**(11), 887 (1984).

-
- [41] W. Yuan, A. Hansen, and Q. Zhang. *Predicting the physical properties of biodiesel for combustion modeling*. Transactions of the ASAE **46**(6), 1487 (2003).
- [42] M. Lapuerta, J. Rodríguez-Fernández, and O. Armas. *Correlation for the estimation of the density of fatty acid esters fuels and its implications. a proposed biodiesel cetane index*. Chemistry and physics of lipids **163**(7), 720 (2010).
- [43] W. Hallett and N. Clark. *A model for the evaporation of biomass pyrolysis oil droplets*. Fuel **85**(4), 532 (2006).
- [44] R. Kolodnytska, M. Al Qubeissi, and S. S. Sazhin. *Biodiesel fuel droplets: transport and thermodynamic properties*. In *Proceedings of the ILASS-Europe* (2013).
- [45] S. K. Jha, S. Fernando, and S. F. To. *Flame temperature analysis of biodiesel blends and components*. Fuel **87**(10), 1982 (2008).
- [46] S. R. Turns *et al.* *An introduction to combustion*, vol. 287 (McGraw-hill New York, 1996).
- [47] N. Hashimoto, H. Nomura, M. Suzuki, T. Matsumoto, H. Nishida, and Y. Ozawa. *Evaporation characteristics of a palm methyl ester droplet at high ambient temperatures*. Fuel **143**, 202 (2015).
- [48] A. Castellanos. *Electrohydrodynamics, international centre for mechanical sciences: Course and lectures-no. 380* (1998).
- [49] P. Atten. *Electrohydrodynamic instability and motion induced by injected space charge in insulating liquids*. IEEE Transactions on Dielectrics and Electrical Insulation **3**(1), 1 (1996).
- [50] P. Vazquez, G. Georgiou, and A. Castellanos. *Numerical analysis of the stability of the electrohydrodynamic (ehd) electroconvection between two plates*. Journal of Physics D: Applied Physics **41**(17), 175303 (2008).
- [51] R. Chicón, A. Castellanos, and E. Martin. *Numerical modelling of coulomb-driven convection in insulating liquids*. Journal of Fluid Mechanics **344**, 43 (1997).

- [52] A. Kourmatzis and J. Shrimpton. *Electrohydrodynamic inter-electrode flow and liquid jet characteristics in charge injection atomizers*. Experiments in fluids **55**(3), 1688 (2014).
- [53] A. Kourmatzis and J. Shrimpton. *Turbulent three-dimensional dielectric electrohydrodynamic convection between two plates*. Journal of Fluid Mechanics **696**, 228 (2012).
- [54] A. Kourmatzis and J. S. Shrimpton. *Characteristics of electrohydrodynamic roll structures in laminar planar couette flow*. Journal of Physics D: Applied Physics **49**(4), 045503 (2015).